Title	A dual finite volume method scheme for catastrophic flash floods in channel networks
Author(s)	Yoshioka, Hidekazu; Unami, Koichi; Fujihara, Masayuki
Citation	Applied Mathematical Modelling (2015), 39(1): 205-229
Issue Date	2015-01
URL	http://hdl.handle.net/2433/193279
Right	© 2014 Elsevier Inc.
Type	Journal Article
Textversion	author

A dual finite volume method scheme for catastrophic flash floods in channel networks

H. Yoshioka[1], K. Unami[2], and M. Fujihara[3]

[1]Graduate School of Agriculture, Kyoto University, Kitashirakawa-Oiwake-cho, Sakyo-ku, Kyoto 606-8502, Japan.

E-mail: yoshih@kais.kyoto-u.ac.jp (Corresponding author)

Tel: 81-75-753-6160

Fax: 81-75-753-6349

[2]Graduate School of Agriculture, Kyoto University, Kitashirakawa-Oiwake-cho, Sakyo-ku, Kyoto 606-8502, Japan.

E-mail: unami@adm.kais.kyoto-u.ac.jp

[3]Graduate School of Agriculture, Kyoto University, Kitashirakawa-Oiwake-cho, Sakyo-ku, Kyoto 606-8502, Japan.

E-mail: fujihara@adm.kais.kyoto-u.ac.jp

Abstract

This paper develops a new numerical scheme for flash floods based on the one-dimensional shallow water equations in channel networks, referred to as the dual finite volume method (DFVM) scheme. The scheme uses an upwind spatial discretization based on staggered meshes so that the flows in multiply connected channel networks are consistently handled without complicated treatment at junctions. The scheme is firstly examined with a series of test cases including idealized and experimental dam break problems to demonstrate its accuracy and versatility. The scheme is then applied to numerical simulation of a flash flood resulting from an earthquake-induced complete dam failure in Japan. Channels from a reservoir to the downstream rivers are modelled as a multiply connected channel network with non-prismatic cross-sections, steep slopes, and bends. The computational results agree well with the field observations and eyewitness reports. Numerical simulation of alternative scenarios as possible cases is also performed to analyze potential risks of the downstream area.

Keywords: Channel network; dam failure; finite volume method; flash floods; shallow water equations.

1. Introduction

Dams play a central role in basic human activities, such as agriculture and fishery. However,

there are always potential failure risks associated with dams. The consequences of a dam failure can be catastrophic, potentially involving the loss of human life. A huge number of dam failures and resulting flash flood events have occurred throughout history. Singh [1] summarized more than 60 major historical dam failures throughout the world, including the Malpasset Dam failure in France [2] and the St. Francis Dam failure in the United States of America [3], both of which resulted in numerous deaths. Numerical simulation is an essential tool for effective flood risk analysis. Three-dimensional description of flash floods requires the use of a hydrodynamic model such as the Navier–Stokes equations [4, 5]. Although hydrodynamic models exhibit high reproducibility for experimental water flows, such models are computationally very demanding and are still difficult to apply to numerical analysis of flows on natural topography. The most reasonable and efficient alternatives to the hydrodynamic models are the cross-sectionally averaged 1-D and the depth-averaged 2-D shallow water equations (SWEs) with the hydrostatic pressure assumption. Aleixo *et al.* [6] experimentally verified the relevance of the hydrostatic assumption for dam break problems. The SWEs are highly nonlinear and their closed-form solutions are only applicable to a limited number of cases, such as flows in prismatic and frictionless channels [7, 8]. Therefore, numerical methods have generally been used to solve the SWEs in engineering applications.

Shallow water modeling of flash flooding involves a number of difficulties, such as unsteady transcritical flows, irregular bed topography, and wet and dry interfaces. Development of accurate and robust numerical methods capable of solving the SWEs under such severe conditions is a challenging task. Most existing numerical schemes for the SWEs are classified as finite volume method (FVM) schemes with approximate Riemann solvers [9, 10], which use analytical solutions to local Riemann problems in evaluating numerical fluxes on cell interfaces. Toro and Garcia-Navarro [11] extensively reviewed Godunov-type schemes as Riemann solvers and summarized future trends and recommendations for these schemes. Since the conventional Godunov-type scheme is, in general, too diffusive for capturing sudden flow transitions, high-resolution algorithms such as total-variation-diminishing (TVD) reconstruction based on slope limiters [12, 13] and adaptive remeshing [14, 15] must be incorporated. Other high-resolution schemes such as the discontinuous Galerkin finite element method (FEM) scheme [16], the essentially non-oscillatory (ENO) scheme [17], the weighted ENO (WENO) scheme [18], and multi-moment FVM schemes [19] have also been applied to the SWEs. On the other hand, researchers have developed sufficiently accurate numerical schemes without using approximate Riemann solvers or high-resolution algorithms. Sabbagh-Yazdi and Zounemat-Kermani [20] applied a Galerkin FVM scheme to the 2-D SWEs, adding a fourth-order artificial dissipation term as a stabilization technique. Ying *et al*. [21] developed an FVM scheme for dam break problems in non-prismatic and

non-rectangular channels with a weighted average-based water surface treatment. Unami *et al.* [22] developed a cell-centered FVM scheme with a Froude number-based upwind method to predict dam break events in Ghanaian inland valleys, which actually occurred at a later date [23]. A 1-D counterpart of the scheme has also been developed [24].

For rapidly varied flows in steep and narrow channels in the presence of flow bifurcations and conversions in particular, such as river networks and mountainous valleys, the 1-D SWEs are more effective and computationally efficient than the 2-D SWEs [25, 26]. In such cases, the domain of the flow is approximated as a locally one-dimensional open-channel network extending over the horizontally two-dimensional plane. Due to the singularity of the 1-D SWEs at junctions in the domains, appropriate internal boundary conditions are required in order to determine local flow behaviors around the junctions, causing difficulties in implementing high-resolution algorithms. Sanders *et al.* [27] simulated contaminant transport in tidal river networks by nesting a 2D model at junctions, so that the converging and diverging behaviors of the flows are accurately resolved. Capart *et al.* [28] developed a characteristic-based FVM scheme for the 1-D SWEs in natural channels and applied the scheme to flow routing of a typhoon-induced flood event in an existing river network. Kesserwani *et al.* [29] investigated several nonlinear internal boundary condition models for subcritical flows at junctions and compared them with a series of experimental data. Kesserwani *et al.* [30] carried out numerical analysis of free surface water flows at a T-shaped junction in the context of the 1-D SWEs with source terms for discharge and momentum losses by flow divisions. Trancoso *et al.* [31] developed a staggered FVM scheme for open-channel network flows and coupled this scheme with distributed hydrological models. Van Tsang *et al.* [32] applied a lattice Boltzmann method to shallow water flows in a complicated irrigation canal network equipped with hydraulic structures. Zhu *et al.* [33] established an efficient numerical method to deal with backwater effects at junctions based on the method of characteristics. Until now, only a limited number of studies have investigated flows in multiply connected (looped) channel networks with steep, non-rectangular, and non-prismatic channels. Since natural channels are typically irregular and have the above characteristics [34], an appropriate numerical scheme that can consistently deal with junctions and handles rapidly varying flows under severe computational conditions is strongly desired for reliable flash flood simulations.

Recently, Unami and Alam [35] proposed a versatile numerical scheme for rapidly varying flows in multiply connected channel networks, here referred to as the Finite Element/Volume Method (FEVM) scheme. The FEVM scheme applies the standard Galerkin FEM with linear basis and an upwind cell-centered FVM to the continuity equation and to the momentum equation, respectively, so that the flows at junctions are handled consistently. The FEVM

scheme is explicit in time; however, it requires iterative matrix inversions at each time step. Ishida *et al.* [36] have developed a similar numerical scheme that has the same drawback. This study develops a more computationally efficient numerical scheme, referred to as the Dual-FVM (DFVM) scheme, which works effective in preserving monotonic water surface profiles in some transient flows. The continuity equation is defined as a local integral in which junctions are dealt with as the implicit internal boundary conditions. Spatial discretization in the DFVM scheme is based on the concept of Voronoi diagram [37], which has been used to design staggered schemes for different transport equations, such as the 1-D SWEs in single channels [38], the 2-D SWEs [39], the governing equations of three-dimensional hydrostatic free surface water flows [40], and the advection-dispersion equations [41]. Application of the Voronoi diagram to the 1-D SWEs in channel networks has not been presented in the literature. In the DFVM scheme, water surface elevation and discharge are taken as the unknowns arranged in a staggered manner. A non-upwind, vertex-centered FVM and a cell-centered FVM employed in the FEVM scheme with a semi-implicit treatment of the friction slope term are applied to the continuity equation and to the momentum equation, respectively. The DFVM scheme is verified with a number of numerical tests in order to determine its accuracy. Finally, the DFVM scheme is applied to numerical simulation of catastrophic flash flooding that results from a recent earthquake-induced dam failure in Japan.

The remainder of the present paper is organized as follows. In Section 2, a brief introduction of locally one-dimensional open-channel networks and 1-D SWEs is provided. In Section 3, numerical formulation for the DFVM scheme is presented. In Section 4, the DFVM scheme is verified through a number of test problems. In Section 5, the scheme is applied to the numerical simulation of a recent flash flood caused by an earthquake-induced complete dam failure in Japan. Section 6 concludes this study.

2. Mathematical model

2.1 Definition of locally one-dimensional open-channel network

In analyzing free surface water flows propagating along channels, a one-dimensional shallow water approximation has practically been applied to the flow fields [42]. In such a case, a locally one-dimensional open-channel network extending over the horizontal two-dimensional plane gives the domain of flow. A locally one-dimensional open-channel network is a connected graph consisting of a collection of a finite number of reaches linked via a set of vertices. Hydraulic properties, such as the wetted cross-sectional area, water surface elevation, and discharge are distributed on the graph. A finite line gives the reach, and an arbitrary position in the domain is uniquely determined from a local abscissa taken along the reaches. A vertex is called a boundary vertex if it is connected to exactly one reach and is

referred to as a bending point if it is connected to exactly two reaches. Otherwise, the vertex is referred to as a junction. A channel network is said to be multiply connected if it contains at least one loop, and is otherwise said to be simply connected [43]. Partial differential equations, such as the 1-D SWEs defined in locally one-dimensional open-channel networks, generally associate internal boundary conditions at junctions to determine local solution behaviors [44].

2.2 One-dimensional shallow water equations

The 1-D SWEs for free surface water flows along single channels with arbitrary cross-sectional shapes consist of the continuity equation [45]

$$\frac{\partial A(\eta)}{\partial t} + \frac{\partial Q}{\partial x} = q \tag{1}$$

and the momentum equation

$$\frac{\partial Q}{\partial t} + \frac{\partial}{\partial x}\left(\frac{\beta Q^2}{A}\right) = -gA\frac{\partial \eta}{\partial x} - gAS_f \tag{2}$$

where t is the time, x indicates the abscissa, A is the wetted cross-sectional area as a function of the water surface elevation η, Q is the discharge, q is the lateral inflow per unit length of the channel, β is the momentum flux coefficient, g is the gravitational acceleration, and S_f is the friction slope given by Manning's formula

$$S_f = \frac{n^2 Q|Q|P^{4/3}}{A^{10/3}} \tag{3}$$

where n is Manning's coefficient and P is the wetted perimeter. The channel bed elevation z is assumed to be fixed. The conventional SWEs, (1) and (2), can be applied to arbitrary single channels. However, for the flows in channel networks, the continuity equation (1) shall be understood as the integral form

$$\int_{\Omega \cap B(y,r)} T\frac{\partial \eta}{\partial t}dx + \sum_{j=1}^{v}\sigma_j Q_{r,j} + \sum Q_B = \int_{\Omega \cap B(y,r)} qdx \tag{4}$$

where Ω represents the domain of the flow as a locally one-dimensional open-channel network, $T = \frac{\partial A}{\partial \eta}$ is the top width of the water surface, $B(y,r)$ is the horizontally two-dimensional r-neighborhood of a point $y \in \Omega$ with $r > 0$ such that no vertex falls on the boundary of $B(y,r)$, v is the total number of intersections of the reaches and the boundary of $B(y,r)$, $Q_{r,j}$ is the discharge at the jth intersection, $\sum Q_B$ represents the sum of the discharges specified at the boundary vertices in $\Omega \cap B(y,r)$, and σ_j is the sign parameter defining the direction of the abscissa in the jth reach. Here, σ_j is equal to 1 when the

abscissa in the jth reach is facing outward to the boundary of $B(y,r)$ and is otherwise equal

to -1. A schematic diagram of $B(y,r)$ is shown in **Fig. 1**. Note that $B(y,r)$ in (4) can be

replaced by a sufficiently small compact two-dimensional set contained in $B(y,r')$ for

arbitrary $0 < r' < r$. Application of the integral form (4) in single channels recovers the

conventional form (1). The new continuity equation (4) is still conservative and valid for

arbitrary locally one-dimensional open-channel networks.

3. Finite volume formulation

3.1 Computational mesh

The 1-D SWEs comprising the continuity equation (4) and the momentum equation (2) are

numerically solved using the DFVM scheme, with the water surface elevation η and the

discharge Q as unknowns. A couple of staggered computational meshes, which are a regular

mesh and a dual mesh, are used in the scheme. The continuity equation (4) is solved on the

dual mesh, while the momentum equation (2) is solved on the regular mesh, so as to avoid

conflicting numbers of equations and unknowns. The domain Ω is first divided into a regular

mesh consisting of regular cells bounded by two nodes, so that any vertex, such as a junction,

falls on one of the nodes. The regular cells and the nodes are indexed with the natural

numbers. The total numbers of regular cells and nodes are denoted by N_{c} and N_{n},

respectively. The kth regular cell is denoted by Ω_k. The length of Ω_k is represented by l_k.

The two nodes bounding both sides of Ω_k are denoted by the $\varphi(k,1)$th node and the $\varphi(k,2)$

th node. The abscissa in Ω_k is directed to the $\varphi(k,2)$th node. The number of regular cells

connected to a generic ith node is denoted by $\nu(i)$. The jth regular cell connected to the ith

node is referred to as the $\kappa(i,j)$th regular cell $\Omega_{\kappa(i,j)}$. There are two nodes that bound

$\Omega_{\kappa(i,j)}$. One is the ith node, and the other is referred to as the $\mu(i,j)$th node. In $\Omega_{\kappa(i,j)}$, the

direction of the abscissa is identified with the parameter $\sigma_{i,j}$, which is equal to 1 when x is

directed to the $\mu(i,j)$th node, and is otherwise equal to -1. A dual mesh is generated from

the regular mesh. Following the multi-dimensional analogue [37], the ith dual cell S_i is

defined as

$$S_i = \left\{ x \mid \; |x_i - x| < \left| x_{\mu(i,j)} - x \right| \; \text{ for } \; 1 \le j \le \nu(i) \right\} \tag{5}$$

where x_i and $x_{\mu(i,j)}$ represent x at the ith node and at the $\mu(i,j)$th node, respectively. The

dual mesh consists of N_{n} dual cells. The cell interface between S_i and $S_{\mu(i,j)}$ is denoted by

$\Gamma_{i,j}$. **Fig. 2** shows a schematic diagram of the computational mesh. The water surface elevation η is attributed to the dual cells, and the discharge Q is attributed to the regular cells. The discretized η in S_i is denoted as η_i, and the discretized Q in Ω_k is denoted as Q_k. The model parameters n and β are attributed to the regular cells, and model parameters in Ω_k are denoted as n_k and β_k.

3.2 Continuity equation

The continuity equation (4) is discretized on a dual mesh. Replacing $B(y,r)$ with S_i yields the cell-vertex finite volume formulation of the continuity equation in S_i, as follows:

$$\int_{S_i} T \frac{\partial \eta}{\partial t} dx + \sum_{j=1}^{v(i)} \sigma_{i,j} Q_{\Gamma_{i,j}} = \int_{S_i} q dx . \tag{6}$$

Substituting $Q_{\Gamma_{i,j}} = Q_{\kappa(i,j)}$ into (6) yields

$$\int_{S_i} T \frac{\partial \eta}{\partial t} dx + \sum_{j=1}^{v(i)} \sigma_{i,j} Q_{\kappa(i,j)} = \int_{S_i} q dx . \tag{7}$$

Assuming a linear variation of the top width T in $\Omega_{\kappa(i,j)}$ yields

$$T = T_{i,j,0} + \frac{x - x_i}{\sigma_{i,j} l_{\kappa(i,j)}} \left(T_{i,j,1} - T_{i,j,0} \right) \tag{8}$$

where $T_{i,j,0}$ and $T_{i,j,1}$ are the values of T at the ith node and at the $\mu(i,j)$th node in $\Omega_{\kappa(i,j)}$, respectively. According to (8), the first term on the left-hand side of (7) is evaluated as follows:

$$\int_{S_i} T \frac{\partial \eta}{\partial t} dx = \frac{d\eta_i}{dt} \int_{S_i} T dx$$

$$= \frac{d\eta_i}{dt} \int_{S_i} \left(T_{i,j,0} + \frac{x - x_i}{\sigma_{i,j} l_{\kappa(i,j)}} \left(T_{i,j,1} - T_{i,j,0} \right) \right) dx . \tag{9}$$

$$= \left(\frac{1}{8} \sum_{j=1}^{v(i)} l_{\kappa(i,j)} \left(3T_{i,j,0} + T_{i,j,1} \right) \right) \frac{d\eta_i}{dt}$$

Thus, each $\dfrac{d\eta_i}{dt}$ is computed as

$$\frac{d\eta_i}{dt} = \left(-\sum_{j=1}^{v(i)} \sigma_{i,j} Q_{\kappa(i,j)} + \sum q \right) \Bigg/ \left(\frac{1}{8} \sum_{j=1}^{v(i)} l_{\kappa(i,j)} \left(3T_{i,j,0} + T_{i,j,1} \right) \right) \tag{10}$$

where $\sum q$ represents the discharge contributed from the lateral inflows and the boundary conditions.

3.3 Momentum equation

The upwind cell-centered FVM [35] is applied to the momentum equation (2). Then, a semi-implicit discretization method is used to evaluate the friction slope term in order to avoid the numerical instability due to the extremely shallow water depth. The cell-centered finite volume formulation of the momentum equation in the kth regular cell Ω_k leads to

$$l_k \frac{dQ_k}{dt} + [F]_{\partial\Omega_k} = \int_{\Omega_k} gA\left(-\frac{\partial\eta}{\partial x} - S_f\right) dx \tag{11}$$

where $\partial\Omega_k$ is the interface of Ω_k and $F = \dfrac{\beta Q^2}{A}$ is the flux evaluated on $\partial\Omega_k$. Each term of (11) is discretized in the following subsections.

Flux evaluation in the momentum equation (11) is carried out by a simple upwind discretization. For each generic regular cell Ω_k at any time t, the node, of the two nodes bounding Ω_k, to which the flow is directed is referred to as the downstream node, and the other is referred to as the upstream node. The vector starting from the upstream node and ending at the downstream node is denoted by χ_k. The cell flux F_k for the regular cell Ω_k is determined using the local Froude number as a weight. When the downstream node in Ω_k is wet, $A_{k,\mathrm{DS}} \geq \varepsilon$ for a small threshold value ε, and the cell cross-sectional area A_k and the cell cross-sectionally averaged velocity V_k are calculated as

$$A_k = (1 - \omega_k) A_{k,\mathrm{DS}} + \omega_k A_{k,\mathrm{US}} \tag{12}$$

and

$$V_k = \frac{Q_k}{A_k} \tag{13}$$

with the weight

$$\omega_k = \max\left(1 - \frac{1}{Fr_k^2}, 0\right) \tag{14}$$

where Fr_k^2 is the square of local Froude number defined as

$$Fr_k^2 = \frac{\beta_k T_{k,\mathrm{DS}} Q_k^2}{g A_{k,\mathrm{DS}}^3} \tag{15}$$

and the subscripts US and DS indicate values at the upstream node and the downstream node, respectively, in Ω_k. The cell velocity V_k is taken to be 0 when $A_{k,\mathrm{DS}} < \varepsilon$. Then, ε is taken to be sufficiently small because of its influence on wet and dry interfaces, as discussed in Xia *et al.* [46]. Finally, the cell flux F_k is determined as follows:

$$F_k = \beta_k Q_k V_k. \tag{16}$$

8

The flux on the cell interface $\partial\Omega_k$ is evaluated following Unami and Alam [35]. The set of indices of the regular cells, the downstream nodes of which fall on the upstream node of Ω_k, is denoted as U_k. The flux at the upstream cell interface $\partial\Omega_{k,\mathrm{US}} \subset \partial\Omega_k$ is prescribed as

$$F\big|_{\partial\Omega_{k,\mathrm{US}}} = \sum_{\kappa \in U_k} \max\left(\cos\theta_{k,\kappa}, 0\right) F_\kappa \tag{17}$$

where $\theta_{k,\kappa}$ is the angle between $\boldsymbol{\chi}_k$ and $\boldsymbol{\chi}_\kappa$. On the other hand, the flux at the downstream cell interface $\partial\Omega_{k,\mathrm{DS}} \subset \partial\Omega_k$ is identical to the cell flux

$$F_{\partial\Omega_{k,\mathrm{DS}}} = F_k \tag{18}$$

with the exception that

$$F_{\partial\Omega_{k,\mathrm{DS}}} = F_k - \min\left(\cos\theta_{k,\kappa}, 0\right) F_\kappa \tag{19}$$

when the downstream node is connected to exactly two regular cells. Finally, the second term of the left-hand side of (11) is evaluated based on $F_{\partial\Omega_{k,\mathrm{US}}}$ and $F_{\partial\Omega_{k,\mathrm{DS}}}$ while considering the directions of the flows as well as that of the x abscissa. The above flux evaluation method has been verified with experimental dam breaks in bend channels [47] and numerical simulations of very shallow surface water flows in an existing open channel network [35] having a number of loops and bends.

The source terms (on the right-hand side of (11)) are discretized using an upwind method. The first term of the right-hand side of (11) is evaluated as

$$\int_{\Omega_k} gA\left(-\frac{\partial\eta}{\partial x}\right)\mathrm{d}x = -gl_k \overline{A}_k\left(\eta_{\varphi(k,2)} - \eta_{\varphi(k,1)}\right) \tag{20}$$

where

$$\overline{A}_k = \begin{cases} A_{k,\mathrm{US}} & \left(Fr_k^2 \geq 1\right) \\ \dfrac{A_{k,\varphi(k,1)} + A_{k,\varphi(k,2)}}{2} & \left(Fr_k^2 < 1\right) \end{cases}. \tag{21}$$

Next, the friction slope term is discretized in a semi-implicit manner [48] as

$$\int_{\Omega_k} gA\left(-S_\mathrm{f}\right)\mathrm{d}x = -gl_k \overline{A}_k\left(S_{\mathrm{f},k} + \frac{1}{2} J_{S_\mathrm{f},k}\Delta t \frac{\mathrm{d}Q_k}{\mathrm{d}t}\right) \tag{22}$$

with

$$S_{\mathrm{f},k} = \frac{n_k^2 Q_k \left|Q_k\right| \overline{P}_k^{4/3}}{\overline{A}_k^{10/3}} \tag{23}$$

and

$$\overline{P}_k = \begin{cases} P_{k,\mathrm{US}} & \left(Fr_k^2 \geq 1 \right) \\ \dfrac{P_{k,\varphi(k,1)} + P_{k,\varphi(k,2)}}{2} & \left(Fr_k^2 < 1 \right) \end{cases} \tag{24}$$

where $J_{S_\mathrm{f},k}$ is the Jacobean of $S_{\mathrm{f},k}$ with respect to Q_k defined as

$$J_{S_\mathrm{f},k} = \frac{2n_k^2 |Q_k| \overline{P}_k^{4/3}}{\overline{A}_k^{10/3}} . \tag{25}$$

However, S_f is taken as 0 when $\overline{A}_k < \varepsilon$. Finally, each $\dfrac{\mathrm{d}Q_k}{\mathrm{d}t}$ is explicitly computed as

$$\frac{\mathrm{d}Q_k}{\mathrm{d}t} = \frac{1}{l_k \left(1 + \dfrac{1}{2} g \overline{A}_k J_{S_\mathrm{f},k} \Delta t \right)} \left(-[F]_{\partial\Omega_k} - g \overline{A}_k \left(\eta_{\varphi(k,2)} - \eta_{\varphi(k,1)} + l_k S_{\mathrm{f},k} \right) \right). \tag{26}$$

3.4 Temporal integration

Application of the DFVM scheme to the 1-D SWEs finally yields a system of ordinary differential equations (ODEs) for the water surface elevation η attributed to the dual cells and the discharge Q attributed to the regular cells. Boundary conditions are specified at the boundary vertices when necessary, and the system of ODEs is temporally integrated from a prescribed initial condition using the fourth-order Runge–Kutta method. The time increment Δt is chosen to be sufficiently small, so that the Courant–Friedrichs–Lewy condition [49] is satisfied.

3.5 Some remarks

The DFVM scheme is fully explicit in time and does not necessitate matrix inversion algorithm, which on the other hand is required in the FEVM scheme. Therefore, the scheme is considered to be superior to the FEVM scheme in terms of computational efficiency. Indeed, preliminary computations for transient problems showed that the DFVM scheme is two to three times faster than the FEVM scheme. Much faster computation time can be achieved if a lower order time integration method, such as the forward Euler method and the second-order Runge-Kutta method, is employed. Moreover, the DFVM scheme is simpler than the conventional ones because it has a compact stencil in spatial discretization and does not depend on any high-resolution algorithms. Note that the DFVM scheme exactly preserves the water at rest level because it does not involve water surface reconstruction.

4. Numerical tests

Numerical tests containing a tidal wave problem and a series of dam break problems, which have served as important benchmarks [50, 51, 52], are carried out to determine accuracy of

the DFVM scheme. Throughout this section, the momentum flux coefficient β is fixed to 1.0 in every cross-section, and the threshold vale ε is set to be 1.0×10^{-6} (m^2).

4.1 Tidal wave problem in an irregular channel

The DFVM scheme is firstly applied to a tidal wave problem to examine its capability of handling flows with complex bathymetry. A 1,500 (m) long non-prismatic rectangular, frictionless channel is considered as the domain $\Omega = (0,1500)$ (m). Width and bed elevation of the channel is taken from Vázquez-Cendón [51], both of which are continuous but highly irregular. Initial conditions are set as $\eta = 11$ (m) and $Q = 0$ (m^3/s) in the entire domain. Both the upstream and downstream ends are solid walls, but the water surface elevation at the upstream end is specified directly as

$$\eta(t,0) = 15 + 4\sin\left(\pi\left(\frac{4t}{86,400} - \frac{1}{2}\right)\right). \tag{27}$$

Asymptotic solution in the limit of zero Froude number is available in the literature [53, 54]. The domain is divided into 300 uniform regular cells. The time increment is $\Delta t = 0.5$ (s) and computational period is 10,800 (s). Comparison of the computed and analytical discharges per unit width at the time 10,800 (s) is shown in **Fig. 3**. Maximum absolute error between the computed and analytical water surface elevations at the time is 0.03 (%). Therefore, plots for the water surface elevations are not provided.

4.2 Dam break problems in a flat, frictionless rectangular channel

Dam break problems in a flat, frictionless channel are considered. A 2,000 (m) length channel is considered as the domain $\Omega = (0,2000)$ (m). The initial water surface elevation η (m) is

$$\eta = \begin{cases} h_U & (x \le 1000) \\ h_D & (x > 1000) \end{cases} \tag{28}$$

where h_U and h_D denote the initial upstream and downstream water depths, respectively, with $h_U > h_D > 0$. The initial discharge is $Q = 0$ (m^3/s) for the entire domain. The initial upstream water depth h_U is fixed to 1.0 (m), while the initial downstream water depths h_D of 0.1 (m) (Case DB-A) and of 0.0 (m) (Case DB-B) are examined. The boundaries are treated as solid walls. Solution to Case DB-B involves a wet and dry interface, which is difficult to accurately capture even if high-resolutions algorithms are employed [55, 56]. Here, the two cases of $\Delta x = 10$ (m) and $\Delta x = 1$ (m) are investigated. The time increment Δt is fixed to 0.001 (s). The analytical and computed water surface profiles and velocity distributions at $t = 50$ (s) are illustrated in **Figs. 4** through **7** for each case. The computational results are shown to be sufficiently accurate, and the numerical solutions are shown to approach the

11

exact solutions as the mesh is refined. Computational results do not contain spurious oscillations as found in those using the FEVM scheme, and are not inferior to recently published ones slightly underestimating the velocity of the wet and dry interface.

4.3 Dam break problem in a flat, frictionless triangular channel

A dam break problem in a triangular channel is considered in order to determine the accuracy of the DFVM scheme for rapidly varying flows in non-rectangular channels. Sanders [57] investigated dam break problems in non-rectangular channels including triangular channels, and his research was followed up on by several researchers [58, 59]. Shallow water flows in triangular channels are generally difficult to compute compared to flows in rectangular channels since the top width of the cross-section varies in direct proportion to the water depth, which significantly reduces the accuracy of the wave speed of the flows on a dry bed. The test problem here is carried out in the same setting as the previous dam break problem on a dry bed (Case DB-B) except that each cross-section is triangular and has a side gradient of 1:1 and h_U is set to 10 (m). The FEVM scheme has been preliminarily applied to this problem under the same computational conditions; however, positivity of the water depth is violated near the wet and dry interface due to spurious oscillations, which do not disappear even if more fine computational mesh and time increments are used. This indicates limited applicability of the FEVM scheme to transient flows in non-rectangular channels with wet and dry interfaces. **Figs. 8** and **9** show the computational results for the water surface profile and the velocity distribution for this test problem. Convergence of the computed solutions are slower than those of the high-resolution schemes, but preserve monotonicity and positivity of water surface profiles. Here dependence of the computed solutions on the upstream Courant number [57]

$$\mathrm{Cr}_\mathrm{U} = \sqrt{g\,\frac{A(h_\mathrm{U})}{T(h_\mathrm{U})}}\,\frac{\Delta t}{\Delta x} \tag{29}$$

is also investigated. In this test case, $\mathrm{Cr}_\mathrm{U} = 7 \times 10^{-4}$ for the coarse mesh ($\Delta x = 10$ (m)) and $\mathrm{Cr}_\mathrm{U} = 7 \times 10^{-3}$ for the fine mesh ($\Delta x = 1$ (m)). Sanders [57] reported that accuracy of computed solutions increases as Cr_U approaches the order of $O(10^{-1})$, which is consistent with the results presented in Figs 8 and 9.

4.4 Thacker's test case

The DFVM scheme is verified with the Thacker's test case where the analytical solution is available [58, 59]. This problem is a severe test case that involves both advancing and receding wet and dry interfaces on non-flat channel bed. The computational domain Ω is a

frictionless rectangular channel $(-4,000, 4,000)$ (m) in which the bottom elevation z is distributed as

$$z = h_0 \left(\frac{x^2}{a^2} - 1 \right) \text{ (m)} \tag{30}$$

with $h_0 = 10$ (m) and $a = 2,500$ (m). The channel width is set as 1 (m). The initial condition of the water surface elevation η is set as

$$\eta = z + \max\{0, Z(0, x) - z\} \text{ (m)} \tag{31}$$

where $Z = Z(t, x)$ is given by

$$Z(t, x) = \frac{1}{4g} \left(-B^2 - B^2 \cos(2\omega t) - 4B\omega x \cos(\omega t) \right) \text{ (m)} \tag{32}$$

with the parameters $B = 5$ (m/s) and $\omega = 0.0056$ (1/s). The initial condition of the discharge Q is set as 0 (m^3/s) in the entire Ω. The analytical solutions of η and Q for $t > 0$ (s) are given by

$$\eta = z + \max\{0, Z - z\} \text{ (m)} \tag{33}$$

and

$$Q = B \max\{0, Z - z\} \sin(\omega t) \text{ (m}^3\text{/s),} \tag{34}$$

respectively. The two cases of $\Delta x = 10$ (m) and $\Delta x = 5$ (m) are examined to see convergence of the scheme. The time increment Δt is set as $T/4,000$ (s) in the former case and as $T/8,000$ (s) in the latter where $T = 1,121$ (s). The minimum nodal water depth is set as 0.001 (m) to avoid negative water depth encountered at the receding wet and dry interfaces.

Figs. 10(a) through **10(d)** show comparisons of the exact and computed water surface profiles at each time step. Similarly, **Figs 11(a)** through **11(d)** show comparisons of the exact and computed discharges. The computed solutions agree well with the analytical ones, accurately resolving the wet and dry interfaces. The computed η and Q converge to the analytical ones as the mesh is refined.

4.5 Dam break problem in a non-prismatic rectangular channel

Here, the DFVM scheme is validated using a dam break problem in an experimental non-prismatic rectangular channel with a flat and wet bed. Bellos *et al.* [60] conducted a series of experimental dam break problems in a converging and diverging rectangular channel. The experimental channel is shown in **Fig. 12**. Detailed drawings of the channel are summarized in Bellos *et al.* [61]. The channel width of the upstream part of the channel is 1.40 (m). The channel width gradually decreases from 1.40 (m) to 0.60 (m) toward the contraction at

13

$x = 8.5$ (m), where a vertical wall serving as a dam is installed, and gradually increases to 1.40 (m) toward the downstream end, at which a weir is located. The initial upstream and downstream water depths of the dam are set to 0.250 (m) and 0.101 (m). The dam is instantaneously removed at the initial time $t = 0$ (s). As shown in **Fig. 12**, the channel has an asymmetrical shape and the resulting water flow may exhibit a horizontally two-dimensional nature. Nevertheless, as shown in and cross-sectionally averaged modeling has found to be successful in simulating experimental results with satisfactory precision. Tseng *et al*. [48] and Tseng and Yen [62] verified several high-resolution schemes with this test problem. Manning's coefficient n of the channel has been set as 0.012 (s/m$^{1/3}$), as in previous studies [63]. Since the dimensions of the downstream weir are not available, the channel is increased by 9.3 (m), as in Hicks *et al*. [64], and a critical flow condition is specified at the new downstream end. Therefore, reflection waves at the original downstream end cannot be produced. The channel is divided into regular cells of length $\Delta x = 0.1$ (m). The time increment Δt is set to be 0.01 (s). **Fig. 13** illustrates the comparison of computed and measured water depths at the observation stations at $x = 4.5$ (m), $x = 8.5$ (m), and $x = 13.5$ (m). Computational results adequately capture water depth variations due to a moving shock and a depression wave, and do not show significant differences with those of the high-resolution schemes.

4.6 Dam break problem with a triangular bump

The DFVM scheme is verified with the laboratory dam break experiment conducted by Alcrudo and Fazãro [65]. The experimental setting is shown in **Fig. 14**. The channel has a rectangular cross-section of 1.75 (m) wide, and is composed of an upstream reservoir filled with water with the depth of 0.75 (m), and a dry downstream channel with a symmetrical triangular bump with the height of 0.40 (m). The vertical wall installed at $x = 15.5$ (m) is assumed to be instantaneously removed at $t = 0$ (s). The Manning's coefficient n is set to be 0.0125 (s/m$^{1/3}$) as adopted in Liang and Marche [66]. The upstream end is taken as a solid wall and a free outflow condition is specified at the downstream end. This problem involves wet and dry interfaces and receding bores that occur when the discharged water from the reservoir hits the bump. The domain is divided into 190 uniform regular cells. The time increment is $\Delta t = 0.01$ (s). **Fig. 15** shows comparisons of the computed and measured water depths at $x = 19.5$ (m), $x = 25.5$ (m), and $x = 28.5$ (m). Sudden changes of the water depths are well resolved, though with slight overestimations. The computed water depths in **Figs. 15(a)** and **15(b)** involve numerical oscillations, which attenuate in time and therefore do not limit applicability of the present scheme. High-resolution algorithms will suppress these oscillations, but forfeiting the simplicity of the scheme. Computational results are

quantitatively consistent with those using the high-resolution schemes of Liang and Marche [66], Singh *et al.* [67], and Bollermann *et al.* [68], in which the channel is divided into 760, 3,800, and 200 uniform cells along the flow direction, respectively.

4.7 Dam break problems in a non-prismatic and non-flat channel

Hydraulic experiments with a rectangular flume were carried out to examine capability of the DFVM scheme handling dam break problems in non-prismatic and non-flat channels. These experiments are more severe than the preceding two cases because the latter involve only either non-prismatic cross-section or non-flat channel bed. The experimental settings of the presented cases are shown in **Fig. 16.** Length and width of the flume were 20.0 (m) and 0.60 (m), respectively. The channel consisted of an upstream reservoir, an upstream reach, a symmetrical broad crested weir, and a downstream reach with a free outfall. A couple of blocks with a thin gate installed just upstream of them served as a dam to fill up water in the reservoir. A trapezoidal obstacle was installed on the weir to create a 1.20 (m)–long non-prismatic reach having a gradual contraction with the angle of 54.3 (deg) and a 0.25 (m)–wide sudden expansion. Distance between the downstream sides of the obstacle and the top of the weir was 0.06 (m). Height of the obstacle was sufficiently high to serve as a sidewall creating a channel construction on the weir. The two cases of the flume slopes $S = 0$ and $S = 0.01$ were examined. Initially the downstream reach and the top of the weir were dry and the reservoir was filled with still water such that the water depth just upstream of the blocks equals to 0.37 (m). The upstream reach was also filled with still water to serve as a pool whose water surface elevation equals to the elevation of the upstream-side of the top of the weir. The gate was suddenly removed to create a 0.30 (m)–wide partial dam breach. The opening of the gate created a flash flood propagating on the pool before flowing over the weir. The flows downstream of the weir involved a series of oblique hydraulic jumps in both of the test cases due to the sudden expansion of the channel cross-section.

Water depths in the channel were measured with hydrostatic head level gauges with the resolution of 1 (s) (HOBO U-20) at the three stations as shown in **Fig. 16** whose locations were $x = 8.0$ (m) (in the upstream reach), $x = 16.0$ (m) (in the downstream reach), and $x = 20.0$ (m) (at the downstream end), respectively. Traveling time of the flows to the downstream end of the channel were estimated from the measured data and video images as 9.0 (s) with $S = 0$ and 8.0 (s) with $S = 0.01$, respectively. The Manning's coefficient n of the channel has been estimated as 0.01 (s/m$^{1/3}$). The gate is assumed to be instantaneously removed at the initial time $t = 0$ (s). The entire channel is uniformly divided into 1,000 regular cells with the length of 0.02 (m). The time increment Δt is set as 0.005 (s). Response

15

characteristics of the head level gauges as a convolution operator between the true (from video images; input data) and measured water depths (output data) was preliminary estimated with the inverse analysis method using Tikhonov regularization [69]. The computed water depths at the observation stations with the DFVM scheme were then emulated with the estimated convolution operator to create another set of water depths data (emulated data) accounting for the response characteristics of the gauges, which are more appropriate to be compared with the measured results.

Figs. 17(a) through **17(c)** and **Figs. 18(a)** through **18(c)** show comparisons of the computed, emulated, and measured water depths at the three observation stations with the slope $S = 0$ and $S = 0.01$, respectively. These figures show that both the computed and emulated solutions have reasonable phase and amplitude accuracy. They well capture the gradual decreasing of the water depths at all the stations in both of the computational cases. The emulated ones present superior accuracy at the station $x = 8.0$ (m) in particular, demonstrating potential validity of the 1-D SWEs to the dam break problems which cannot be assessed without the emulation technique. Traveling time of the wet and dry interface to the downstream end of the channel with the emulated solutions were 8.7 (s) with $S = 0$ and 7.2 (s) with $S = 0.01$, respectively, reproducing the observed values with slight underestimations. Discrepancies between the numerical and measured results are considered due to the inherently 2-D natures of the flows created by the concrete blocks and the obstacle in the channel. Another possible cause of the discrepancies is the dispersivity of the flows resulting from non-hydrostatic effects, which is not appropriately handled by the SWEs. Despite these limitations of the 1-D SWEs, the computational results with the DFVM scheme are satisfactory accurate, indicating its applicability to dam break problems both with non-prismatic cross-section and non-flat channel bed.

4.8 Dam break problem in a multiply connected channel network with a rectangular cross-section

In this and the next subsections, additional numerical test cases are performed to assess convergence and robustness of the DFVM scheme through the application of dam break problems in multiply connected channel networks. These test problems are challenging because they require a stable discretization method for unsteady transcritical flows of extremely shallow depth as well as a consistent junction treatment technique. Only a few attempts at cross-sectionally averaged modeling have been made for dam break problems in multiply connected channel networks with bends. **Fig. 19** illustrates a plane view of the channel network as the computational domain with key nodes labeled alphabetically from A

to F. The key nodes are referred to as the upstream end (A), the downstream end (E), the bifurcation point (B), the converging point (D), and the bending points (C and F). The reaches have a rectangular cross-sectional shape and are equal in terms of length, Manning's coefficient, and bed slope, which are 10 (m), 0.03 (s/m$^{1/3}$), and 0.01, respectively. The channel width is set to 0.25 (m) in reaches B-F-D, and 0.5 (m) in the other reaches. A vertical wall serving as a dam is installed at the middle of reach A-B, dividing the computational domain into an upstream reservoir and a downstream channel network. The water depth just upstream of the dam is 2.0 (m) and the channel network downstream of the dam is initially dry. Both the upstream and downstream ends are solid walls. The dam is instantaneously removed at the initial time $t = 0$ (s). Each reach is divided into regular cells of length $\Delta x = 0.25$ (m), and the time increment Δt is fixed to 0.001 (s). The numerical solution with $\Delta x = 0.05$ (m) and $\Delta t = 0.00025$ (s) is regarded as the reference solution because no analytical solution is available. **Fig. 20** compares the computed and reference water surface profiles in reaches A-B-C-D-E and B-F-D at each time step. The surge from the reservoir is divided at junction B, taking the local minimum water depth at that point. These divided flows converge at junction D and hit the downstream wall, generating a receding bore. There are also other receding bores starting at bending points C and F, as observed in the experimental dam break problems in bend channels [70]. The flood arrival time at downstream end E is $t = 24.0$ (s). The computed solution is slightly diffusive but exhibits only minor numerical oscillations and is sufficiently close to the reference solution, despite the fact that a coarse computational mesh was used.

4.9 Dam break problem in a multiply connected channel network with a triangular cross-section

Numerical simulation of a dam break problem in a multiply connected channel network with a triangular cross-section is carried out in order to further validate the DFVM scheme. The computational conditions are identical to those of the previous dam break problem, except that each cross-section is triangular and the water depth upstream of the dam is 1.0 (m). The side gradient of the cross-section is $1:\sqrt{3}$ in reaches B-F-D and is 1:1 in the other reaches. **Fig. 21** compares the computed and reference water surface profiles in reaches A-B-C-D-E and B-F-D at each time step. The flood arrival time at downstream end E is $t = 24.5$ (s). As in the previous test problem, the computed water surface profiles are reasonably close to the reference profiles with respect to resolving the receding bores. The computational results of this and the previous test problems show a sufficiently high capability of the DFVM scheme to handle dam break problems in multiply connected channel networks.

5. Application to a recent flash flood caused by a dam failure

The verified DFVM scheme is now applied to the numerical simulation of a recent flash flood event caused by the failure of Fujinuma Dam in Japan.

5.1 Study area

Fujinuma Dam was an earth fill dam that formed Fujinuma Reservoir, in Sukagawa City, Fukushima Prefecture, Japan (N37.302, E140.195; WGS84). Fujinuma Reservoir was used as an irrigation tank for a downstream command area of 850 (ha). The maximum storage capacity of the reservoir was 1,500,000 (m^3). **Fig. 22** shows a map of the study area. Taki Village is northeast of the reservoir, and a paddy field area and Naganuma Village are located southeast of the reservoir. At present, no details on the design and construction history of Fujinuma Dam are available, except for very limited information provided in several recent reports [71, 72]. According to these reports, the construction of Fujinuma Dam began in 1937 and was completed in 1949. **Fig. 23** shows the main and auxiliary embankments of Fujinuma Dam. The dimensions of the main and auxiliary embankments are summarized in **Table 1**. As shown in **Figs. 22** and **23**, Taki Village was located just downstream of the main embankment. According to Kokusyou [73], Fujinuma Dam was built after the settlement of Taki Village regardless of the potential risk of dam failure. Fujinuma Dam was probably not well compacted because modern compaction machines were not available during its construction. Fujinuma Dam was repaired from 1977 to 1999, but the safety factor of the dam at that time has been estimated to be 1.15, which was still less than the required value of 1.20 [74].

Fujinuma Reservoir was significantly damaged by the Great East Japanese Earthquake that occurred on March 11, 2011, which had a maximum magnitude of 9.0. The epicenter of this earthquake was approximately 240 km from the reservoir [75]. The seismic intensity observed at Sukagawa City was reported to be 5 to 6 [76]. The return period of the earthquake was estimated to be 1,000 years [77]. In anticipation of the upcoming irrigation season, Fujinuma Reservoir was filled almost to capacity at the time of the earthquake. The main embankment completely failed due to the earthquake, which resulted in the uncontrolled release of the entire content of the reservoir, and Taki Village was critically struck by the surge from the reservoir. According to a local media report, the surge had a water depth of at least several meters when it struck the village. Consequently, 19 houses were washed away or destroyed, 155 houses were flooded below floor level, and eight people were killed [78]. Kokusyou [73] reported that the flooding in Taki Village lasted at least an hour. EERI (2012) concluded that the main embankment begun breaching within 20 minutes after the earthquake, and complete overtopping of the dam occurred several minutes later. Both Harder *et al.* [79] and Pradel *et al.* [80] inferred that an immediate cause of the complete failure of the main embankment was

a large drop in the crest elevation due to an earthquake-induced landslide. Harder *et al.* [79] also conjectured that the surge from the reservoir traveled downstream along the valley to the northeast until flowing into the Sunoko River and struck Taki Village, before turning 90 degrees to the southeast along the river channel. Kyokawa *et al.* [81] carried out a field survey in the valley downstream of the main embankment and estimated the surge speed to be approximately 10 (m/s). The auxiliary embankment had not failed at the time of the earthquake, but a small arc-shaped deformation of the slope immediately adjacent to the embankment has been reported [72, 82, 83].

5.2 Computational Cases

As described in the previous subsection, in actuality, only the main embankment failed due to the earthquake. However, a significant portion of the paddy field area could have been affected by the flood in the case in which the auxiliary embankment failed. In fact, several observation results [72, 82, 83] have indicated that there was a risk of failure of the auxiliary embankment. Therefore, it is worth considering such alternative scenarios as possible cases of more significant damages to the area downstream of the reservoir than that which actually occurred. Hence, the present study considers three possible scenarios:

Case FDB-A: only the main embankment failed.
Case FDB-B: only the auxiliary embankment failed.
Case FDB-C: both the main and auxiliary embankments failed simultaneously.

In Cases FDB-A and FDB-B, the reservoir water is discharged from the main and auxiliary embankments, respectively. On the other hand, in Case FDB-C, the reservoir water is discharged separately from both of the embankments. Case FDB-A corresponds to the event that actually occurred, and the other cases are hypothetical scenarios.

5.3 Computational mesh

The computational mesh for the flood simulation is determined from a 1:25,000 scale map, aerial view of the flood flow path [88] and satellite image data and digital elevation data obtained from Google Earth (Google Inc., Mountain View, Calif.). **Fig. 24** illustrates the computational mesh with key nodes alphabetically labeled A through K. The total numbers of regular cells and dual cells of the computational mesh are $N_c = 327$ and $N_n = 327$, respectively. The channel network consists of Fujinuma Reservoir (A-B-C and B-G), the valley downstream of the main embankment (C-D), the valley downstream of the auxiliary embankment (G-H), Sunoko River (J-D-E), Kouka River (K-I-E-F), and the paddy field area

(H-I). Nodes A, J, and K are upstream ends and node F is the downstream end. Node E is the conversion point at which the Sunoko River joins the Kouka River. Node D is considered to serve as the representative point of Taki Village, at which the surge from the main embankment hit the village. Node H is the upstream end of the paddy field area. The main and auxiliary embankments, respectively, fall on nodes C and G. Reach H-I is determined so that the flow channel partially varies in accordance with the drainage canals running in the paddy field area. The computational mesh is highly non-uniform, and the maximum and minimum lengths of the regular cells are 201 (m) and 6 (m), respectively. The maximum bed slope of the channel is 0.23 in valley G-H. Each channel cross-section is approximated as a compound shape, as shown in **Fig. 25**, where B is the channel bed width, H_c is the channel height, M_0 is the side slope of the channel, and M_l and M_r are the parameters that account for flooding of the channels. The cross-sections of the dam and the valleys in particular are given as rectangular ($M_0 = 0$ and $H_c = +\infty$) and triangular shapes ($B = 0$ and $H_c = +\infty$), respectively.

5.4 Model parameters

The 1-D SWEs have two model parameters, which are Manning's coefficient n and the momentum flux coefficient β. These model parameters are considered to vary depending on local flow structures, and their estimation is a particularly difficult problem for natural channels with compound cross-sections [84]. Therefore, the present study regards them as global constants rather than local variables. Thus, Manning's coefficient n is set as a moderate constant value everywhere in the domain. Preliminary computations for several values of n within the range of 0.030 to 0.050 (s/m$^{1/3}$) revealed that the computed flow fields have a qualitatively similar nature, except for the differences in flood attenuation and delay. Since the main focus of the numerical simulation here is the verification of the DFVM scheme, Manning's coefficient n is fixed to 0.040 (s/m$^{1/3}$). The momentum flux coefficient β is set to 1.1 because the cross-sectional shape has little complexity. The threshold value ε is chosen as 1.0×10^{-6} (m^2).

5.5 Initial and boundary conditions

Initial and boundary conditions are determined empirically because of the lack of available hydrological data. The paddy field area is assumed to be dry initially because the actual dam failure occurred during the pre-irrigation period in Japan. The valleys are also assumed to be dry initially. The rivers are initially assumed to be in a steady state, such that the water depth does not exceed H_c and remains moderate. Thus, the inflow discharge 10 (m^3/s) is prescribed

at upstream ends J and K. The reservoir is initially assumed to be at full capacity, with a maximum water depth of 18.5 (m). The main and auxiliary embankments are instantaneously and completely removed at the initial time $t = 0$ (s) in each case. Although instantaneous and complete dam removal is not a realistic assumption, it serves as the worst-case failure and allows the earliest bound of the flood arrival time to be assessed [85]. Upstream end A is treated as a solid wall. A critical flow condition is specified at downstream end D, where a hydraulic drop is installed. The time increment Δt is fixed to 0.001 (s). Flow computation for each case is continued until $t = 10,800$ (s).

5.6 Computational results

Fig. 26 shows hydrographs at nodes D, F, and H for each case. The immediate, sharp rise in the hydrograph at D in this case implies that the people in Taki Village did not have sufficient time to evacuate before the flooding. The computed flood arrival time at node D in Case FDB-A is 95 (s), and the average surge velocity in valley C-D is calculated to be 12 (m/s), which is close to the estimated result [81]. The maximum water depth at node D is more than 9 (m) in Case FDB-A, which exceeds the channel depth by more than 4 (m), which also agrees well with eyewitness reports and field survey results [78]. Only slight differences are found between the hydrographs at node D for Cases FDB-A and FDB-C, despite the reservoir water being discharged separately from the two embankments in the latter case. In Case FDB-C, the ratio of the total discharged water volume from the main embankment to that discharged from the auxiliary embankment is 2.5:1.0. The maximum water depth at node H is approximately 8 (m) for both Cases FDB-B and FDB-C. Hydrograph attenuation due to the divided discharge of the reservoir water in Case FDB-C is remarkable at node H, compared to that at node D. These computational results indicate that a reduction in flood damage is actually expected in Case FDB-C. However, the maximum water depth at Taki Village (node D) and the paddy field area (node H) do not significantly decrease, even when both of the embankments failed simultaneously.

Figs. 27(a) through **27(d)** show the water surface profiles for Case FDB-C at the peak discharge from the reservoir ($t = 28$ (s)), the peak water depth at nodes H ($t = 108$ (s)), D ($t = 228$ (s)), and F ($t = 1915$ (s)), respectively, where the channel bottom elevation at node F is taken as 0. Flood propagation in the channel network is reasonably simulated without numerical failure, which demonstrates the robustness of the developed numerical scheme.

Figs. 28(a) through **28(c)** show the distributions of the inundation time, which is defined as the total time that the water depth exceeds the channel depth H_c, for the rivers and the paddy

field area for each case. The inundation time along the Sunoko River is approximately an hour for Cases FDB-A, which is compatible with the observed facts. The inundation time for the paddy field area in Case FDB-B is more than two hours. In Case FDB-C, the inundation time along the Sunoko River and in the paddy field area is at least half an hour. In this case, the paddy field area suffers from flooding for more than an hour. **Figs. 29(a)** through **29(c)** show inundation maps for each case. The inundation areas for Cases FDB-A, FDB-B, and FDB-C are 3.03 (km^2), 2.15 (km^2), and 3.94 (km^2), respectively. Figs. 23 and 24 show that partially non-flooded channels exist in the Kouka River in Case FDB-C, whereas the river is completely flooded in Case FDB-B. The Sunoko River is completely flooded in Cases FDB-A and FDB-C, and a large portion of the paddy field area is inundated in Cases FDB-B and FDB-C.

Overall, the computational results are compatible to the actual flood event. The computational results for Case FDB-C in particular indicate a potential risk of serious flooding in the downstream area, even when the reservoir water is released separately from two embankments.

At present, Fujinuma Reservoir remains damaged. Restoration of the reservoir will be necessary in order to secure an irrigation water supply for rice farming in the study area. However, the computational results clearly show flood risks for the dam downstream area and indicate that extensive discussion is necessary so as to carefully manage Fujinuma Reservoir in order to minimize hazard and failure risk.

6. Conclusions

The present study developed a new numerical scheme for flash floods in channel networks. The DFVM scheme was first presented for efficient numerical resolution of the 1-D SWEs in locally one-dimensional open-channel networks. The continuity equation was formulated in an integral form so that flows around junctions could be handled consistently. The DFVM scheme uses a novel staggered discretization method, in which a vertex-centered FVM is applied to the continuity equation, while an upwind cell-centered FVM is applied to the momentum equation, thereby avoiding conflicting numbers of equations and unknowns. A semi-implicit discretization is employed in the evaluation of the friction slope term in order to cope with flows of extremely shallow water depth. Accuracy of the scheme was verified using a series of test problems. The scheme successfully produced numerical solutions for the dam break problems in multiply connected channel networks, which were challenging problems. Finally, the DFVM scheme was applied to the numerical simulation of the flash flood resulting from the Fujinuma Dam failure considering three scenarios, in which only the main

embankment failed, only the auxiliary embankment failed, and both the main and auxiliary embankments failed simultaneously. Flow channels from Fujinuma Reservoir to the downstream rivers were modeled as a computational domain, which involves non-prismatic and compound channel cross-sections, steep slopes, channel bifurcations and conversions, and sharp bends. The DFVM scheme computed flood propagations in the domain reasonably well. The computational results indicated a high potential flood risk of the reservoir downstream area and suggested the necessity of careful planning with respect to the restoration of Fujinuma Dam.

The numerical scheme presented in the present study is simple, robust, and computationally efficient. Rapidly varying flows in channel networks are consistently dealt with and are adequately simulated without numerical failure. The proposed scheme is considered to serve as an effective tool for numerical simulation and risk analysis of flash floods caused by dam failures.

References
[1] V.P. Singh, *Dam Breach Modeling Technology*. Kluwer academic Publications, 1996, 6-100.

[2] A. Valiani, V. Caleffi, A. Zanni, Case study: Malpasset dam-break simulation using a two-dimensional finite volume method. *J. Hydraulic Eng*. **128**(5) (2002) 460-472.

[3] L. Begnudelli, B.F. Sanders, Simulation of the St. Francis dam-break flood. *J. Eng. Mech.* **133**(11) (2007) 1200-1212.

[4] C. Biscarini, S. Di Francesco, S. Manciola, CFD modelling approach for dam break flow studies. *Hydrol. Earth Syst. Sc*. **14**(4) (2010) 705-718.

[5] C. Yang, B. Lin, C. Jiang, Y. Liu, Predicting near-field dam-break flow and impact force using a 3D model. *J. Hydraulic Res*. **48**(6) (2011) 784-792.

[6] R. Aleixo, S.S. Fazãro, Y. Zech, Velocity-field measurements in a dam-break flow using a PTV Voronoï imaging technique. *Exp. Fluids* **50**(6) (2011) 633-1649.

[7] J.J. Stoker, *Water waves*. Interscience publishing, New York, 1957, 291-341.

[8] Y. Chen, C. Wu, B. Wang, B. Similarity solution of dam-break flow on horizontal frictionless channel. *J. Hydraulic Res*. **49**(3) (2012) 384-387.

[9] P. Roe, Approximate Riemann solvers, parameter vectors, and difference schemes. *J.*

Comput. Phys. **43**(2) (1981) 357-372.

[10] S. Osher, F. Solomon, Upwind difference schemes for hyperbolic systems of conservation laws. *Math. Comput.* **38**(158) (1982) 339-374.

[11] E.F. Toro, P. Garcia-Navarro, Godunov-type methods for free-surface shallow water flows: A review. *J. Hydraulic Res.* **45**(6) (2007) 736-751.

[12] B. Van Leer, Towards the ultimate conservative difference scheme II: Monotonicity and conservation combined in a second order scheme. *J. Comput. Phys.* **14**(4) (1974) 361-370.

[13] A. Harten, P. Lax, B. Van Leer, B. On upstream differencing and Godunov-type schemes for hyperbolic conservation laws. *SIAM Review* **25**(1) (1983), 35-61.

[14] L. Begnudelli, B.F. Sanders, S.F. Bradford, Adaptive Godunov-based model for flood simulation. *J. Hydraulic Eng.* **134**(6) (2008) 714-725.

[15] S. Popinet, Quadtree-adaptive tsunami modeling. *Ocean Dyn.* **61**(9) (2011) 1261-1285.

[16] Y. Xing, X. Zhang, C.S. Shu, Positivity-preserving high order well-balanced discontinuous Galerkin methods for the shallow water equations. *Adv. Water Resour*. **33**(12) (2010) 1476-1493.

[17] A. Scott, P.M.S.V. Rao, A non-oscillatory scheme for open channel flows. *Adv. Water. Resour.* **22**(2) (1998) 133-143.

[18] R. Akoh, S. Ii, F. Xiao, A CIP/multi-moment finite volume method for shallow water. *Int. J. Numer. Methods Fluids* **56**(12) (2008) 2245-2270.

[19] Y. Xing, C.W. Shu, High order finite difference WENO schemes with the exact conservation property for the shallow water equations. *J. Comput. Phys.* **208**(1) (2005) 206-227.

[20] S.R. Sabbagh-Yazdi, M. Zounemat-Kermani, Numerical solution of tidal currents at marine waterways using wet and dry technique on Galerkin finite volume algorithm. *Comput. Fluids*. **38**(10) (2009) 1876-1886.

[21] X. Ying, A.A. Khan, and S.S.Y. Wang, An Upwind Method for One-Dimensional Dam Break Flows", Proceedings of 30th IAHR congress, THEME C: Dam Break (2003) 245-252.

[22] K. Unami, T. Kawachi, G. Kranjac-Berisavljevic, F.K. Abagale, S. Maeda, J. Takeuchi, Case study: Hydraulic modeling of runoff processes in Ghanaian inland valleys. *J. Hydraulic Eng.* **135**(7) (2009) 539-553.

[23] K. Unami, M. Yangyuoru, A.H.M.B. Alam, Ratonalization of buildong mocro-dams equipped with fish passage in West African savannas. *Stoch. Environ. Risk Assess.* **26** (2012) 115-126.

[24] K. Unami, K. Ishida, T. Kawachi, S. Maeda, J. Takeuchi, Stochastic model for behavior of fish ascending an agricultural drainage system. *Paddy Water Environ*. **8**(2) (2010)

105-111.

[25] F. Alcrudo, J. Mulet, Description of the Tous dam break case study (Spain). *J Hydraulic Res*. **45**(Extra Issue) (2007) 45-57.

[26] M. Pilotti, A. Maranzoni, M. Tomirotti, G. Valerio, 1923 Gleno Dam break: Case study. *J. Hydraulic Eng*. **137**(4) (2011) 480-492.

[27] B.F. Sanders, C.L. Green, A.K. Chu, S.B. Grant, Case study: Modeling tidal transport of urban runoff in channels using the finite volume method. *J. Hydraulic Eng*. **127**(10) (2001) 795-804.

[28] H. Capart, T.I. Eldho, S.Y. Huang, D.L. Young, Y. Zech, Treatment of natural geometry in finite volume river flow computations. *J. Hydraulic Eng*. **129**(5) (2002) 385-393.

[29] G. Kesserwani, R. Ghostine, J. Vazquez, R. Mosé, M. Abdallah, A. Ghenaim, Simulation of flow at open-channel junction. *Adv. Water Resour*. **31**(2) (2008) 287-297.

[30] G. Kesserwani, J. Vazquez, N. Rivière, Q. Liang, G. Travin, R. Mosé, New approach for predicting flow bifurcation at right-aligned open channel junction. *J. Hydraulic Eng*. **136**(9) (2010) 662-668.

[31] A.R. Trancoso, F. Braunschweig, P.C. Leitao, M. Obermann, R. Neves, An advanced modeling tool for simulating complex river systems. *Science Total. Environ*. **407**(8) (2009) 3004-3016.

[32] P. Van Thang, B. Chopard, L. Lefèvre, D.A. Ondo, E. Mendes, Study of the 1D lattice Boltzmann shallow water equation and its coupling to build a canal network. *J. Comput. Phys*. **229**(19) (2010) 7373-7400.

[33] D. Zhu, Y. Chen, Z. Wang, Z. Liu, Simple, robust, and efficient algorithm for gradually varied subcritical flow simulation in general channel networks. *J. Hydraulic Eng*. **137**(7) (2011) 766-774.

[34] M. Catella, E. Paris, L. Solari, Conservative scheme for numerical modeling of flow in natural geometry. *J. Hydraulic Eng*. **134**(6) (2008) 736-748.

[35] K. Unami, A.H.M.B. Alam, Concurrent use of finite element and finite volume methods for shallow water equations in locally 1-D channel networks. *Int. J. Numer. Methods Fluids* **69**(2) (2012) 255-272.

[36] K. Ishida, M. Yangyuoru, K. Unami, T. Kawachi, Application of shallow water equations to analyze runoff processes in hilly farmlands. *Paddy Water Environ*. **9**(4) (2011) 393-401.

[37] I.D. Mishev, Finite volume methods on Voronoi meshes. *Numer. Methods Partial Differ. Equat*. **14**(2) (1998) 193-212.

[38] G.S. Stelling, S.P.A. Duinmeijer, A staggered conservative scheme for every Froude number in rapidly varied shallow water flows. *Int. J. Numer. Methods Fluids*, **43**(12) (2012) 1329-1354.

[39] V. Casulli, A high-resolution wetting and drying algorithm for free surface hydrodynamics. *Int. J. Numer. Methods Fluids* **60**(4) (2009) 391-408.

[40] W. Boscheri, M. Dumbser, M. Righetti, A semi-implicit scheme for 3D free surface flows with high-order velocity reconstruction on unstructured. *Int. J. Numer. Methods Fluids* (2013) **72**(6) 607-631.

[41] H. Yoshioka, K. Unami, A cell-vertex finite volume scheme for solute transport equations in open channel networks. *Prob. Eng. Mech*. **31** (2013) 30-38.

[42] R. Szymkiewicz, *Numerical modeling in open channel hydraulics*. Springer, 2010, 301-365.

[43] M. B. Abbott, *Computational hydraulics: Elements of theory of free surface flows*. Pitman, 1979, 267-311.

[44] H. Yoshioka, K. Unami, T. Kawachi, Partial differential equation model for spatially distributed statistics of contaminant particles in locally one-dimensional open channel networks. Proceedings of Tenth International Conference on Hydroscience and Engineering (2012) 24pp.

[45] J.A. Cunge, F.M. Holly, A. Verwey, *Practical Aspects of Computational River Hydraulics*, Pitman, 1980, pp. 7-52.

[46] J. Xia, R.A. Falconer, B. Lin, G. Tan, Modeling flood routing on initially dry beds with the refined treatment of wetting and drying. *Int. J. River Basin Management* **8**(3-4) (2010) 225-243.

[47] K. Ishida, K. Unami, T. Kawachi, Application of one-dimensional shallow water model to flows in open channels with bends. *J. Rainwater Catchment Syst.* **17**(2) (2012) 15-23.

[48] M.H. Tseng, Explicit finite volume non-oscillatory schemes for 2D transient free-surface flows. *Int. J. Numer. Methods Fluids* **30**(7) (1999) 831-843.

[49] E.F. Toro, *Shock-capturing methods for free-surface shallow flows*. Wiley, U.S (2001) 151-171.

[50] P. Garcia-Navarro, A. Fras, I. Villanueva, Dam-break flow simulation: some results for one-dimensional models of real cases. *J. Hydrol.* **216**(3-4) (1999), 227-247.

[51] M.L. Vázquez-Cendón, Improved treatment of source terms in upwind schemes for the shallow water equations in channels with irregular geometry. *J. Comput. Phys.* **148**(2) (1999) 11-34.

[52] C. Zoppou, S. Roberts, Explicit schemes for dam-break flows. *J. Hydraulic Eng.* **129**(1) (2003) 11-34.

[53] T.C. Rebollo, A.D. Delgado, E.D.F. Nieto, A family of stable numerical solvers for the shallow water equations with source terms. *Comput. Methods Appl. Mech. Engrg*. **192**(1-2) (2003) 203-225.

[54] A. Deponti, L. Bonaventura, G. Rosatti, G. Garegnani, An accurate and efficient sami-

implicit method for section averaged free surface flow modelling. MOX-Report No.12/2007 (2007) 32pp.

[55] M. Venutelli, A third-order explicit central scheme for open channel flow simulations. *J. Hydraul. Res.* **44**(3) (2010) 402-411.

[56] C. Ouyang, S. He, Q. Xu, Y. Luo, W. Zhang, A MacCormack-TVD finite difference method to simulate the mass flow in mountainous terrain with variable computational domain, *Comput. Geosci.* **52**(2013) 1-10.

[57] B.F. Sanders, High-resolution and non-oscillatory solution for the St Venant equations in non-rectangular and non-prismatic channels. *J. Hydraulic Res.* **39**(3) (2001) 321-330.

[58] W.C. Thacker, Some exact solutions to the nonlinear shallow-water wave equations. *J. Fluid Mech.* 107(5) (1981) 499-508.

[59] X. Ying, A.A. Khan, S.S.Y. Wang, Upwind conservative schemes for the Saint Venant equations. *J. Hydraulic Eng.* **130**(10) (2004) 977-987.

[60] C.V. Bellos, J. V. Soulis, J.G. Sakkas, Experimental investigation of two-dimensional dam-break induced flow. *J. Hydraulic Res.* **30**(1) (1992) 47-63.

[61] C.V. Bellos, J. V. Soulis, J.G. Sakkas, Computation of two-dimensional dam-break-I nduced flows. *Adv. Water Resour.* **14**(1) (1991) 31-41.

[62] M.H. Tseng, C.L. Yen, Evaluation of some flux-limited high-resolution schemes for dam-break flows with source terms. *J. Hydraul. Res.* **42**(5) (2004) 507-516.

[63] W. Lai, A.A. Khan, Discontinuous Galerkin method for 1D shallow water flow in nonrectangular and nonprismatic channels. *J. Hydraulic Eng.* **138**(3) (2012) 285-296.

[64] F.E. Hicks, P.M. Steffler, M. Yasmin, One-dimensional dam-break solutions for variable width channels. *J. Hydraulic Eng.* **123**(5) (1997) 464-468.

[65] F. Alcrudo, S. Fazãro, Conclusions of the 1st CADAM Meeting-Wallingford, UK, Proceedings of the CADAM Meeting Wallingford, 1999, pp. 35-43.

[66] Q. Liang, F. Marche, Numerical resolution of well-balanced shallow water equations with complex source terms. *Adv. Water. Resour.* **32**(6) (2009) 873 -884.

[67] J. Singh, M.S. Altinakar, Y. Ding, Two-dimensional numerical modeling of dam-break flows over natural terrain using a central explicit scheme. *Adv. Water. Resour.* **34**(10) (2011) 1366-1375.

[68] A. Bollermann, G. Chen, A. Kurganov, S. Noelle, A well-balanced reconstruction of wet/dry fronts or the shallow water equations. *J. Sci. Comput.* **56**(2) (2013) 267-290.

[69] A. Kirsch, *An Introduction to the Mathematical Theory of Inverse Problems.* Springer-Verlag NewYork, 1996, 23-124.

[70] S.S. Fazãro, Y. Zech, Effects of a sharp bend on dam-break flow. Proceedings of the 28th IAHR congress (1999) 7pp.

[71] EERI, Learning from Earthquakes, Geotechnical Effects of the Mw 9.0 Tohoku, Japan,

Earthquake of March 11, 2011. Earthquake Engineering Research Institute, Special Earthquake report (2011) 29pp.

[72] N. Matsumoto, Amended 4th quick report on dams. Japanese Committee on Large Dams (2011) April 4.

[73] T. Kokusyou, A prompt report of the failure of Fujinuma reservoir dam (in Japanese) (2011) Available at

http://www.civil.chuo-u.ac.jp/lab/doshitu/top/fujinuma_sokuho.pdf   Accessed September 24 2012.

[74] Panel to evaluate the seismic stability of dams and small ponds for agricultural purpose of Fukushima Prefecture, Review of the Cause of Fujinuma-ike Failure (2012). Available at   http://www.jcold.or.jp/e/activity/FujinumaSummary-rev.120228.pdf   Accessed September 17 2012.

[75] USGS (2011) Available at

http://earthquake.usgs.gov/earthquakes/recenteqsww/Quakes/usc0001xgp.php
Accessed September 28 2012.

[76] K. Ono, S. Kazama, S. Kawagoe, Y. Yokoo, Dam break caused by the 2011 off the Pacific Coast of Tohoku Earthquake, Fukushima Prefecture, Japan. J. JSNDS **30**(3) (2011) 359-367 (in Japanese).

[77] S.C. Yim, K.F. Cheung, M.J. Olsen, Y. Yamazaki, Tohoku Tsunami Survey, Modeling and probabilistic load estimation applications. Proceedings of the International symposium on Engineering Lessons Learned from the 2011 Great East Japan Earthquake (2012) 430-443.

[78] Kahoku   Online   Network   (2011).   May,   18,   2011 http://www.kahoku.co.jp/spe/spe_sys1072/20110518_01.htm   Accessed   September   17 2012

[79] L.F. Harder, K.I. Kelson, T. Kishida, R. Kayen, Preliminary Observations of the Fujinuma Dam Failure Following the March 11, 2011 Tohoku Offshore Earthquake, Japan. Geotechnical Extreme Events Reconnaissance Report No. GEER-25.e 2011 (2011)

[80] D. Pradel, J. Wartman, B. Tiwari, Failure of Fujinuma dam during the 2011 Tohoku earthquake. Joint Conference Proceedings of the 9th International Conference on Urban Earthquake/ 4th Asia Conference on Earthquake Engineering (2012) 6pp.

[81] H. Kyokawa, K. Konagai, T. Kiyota, T. Katagiri, Z.A. Kazmi, LIDER measurement of the breached earth-fill dam in the March 11th Great East Japan Earthquake. Proceedings of the International Symposium on Engineering Lessons Learned from the 2011 Great East Japan Earthquake (2011) 973-980.

[82] R. Kayen, Y. Tanaka, H. Tanala, T. Sugano, I.A. Estevez, S.S. Cullenward, W. Yeh, D.

Thomas, LiDAR and field investigation of the March 11, 2011 M9.0 Great Tohoku offshore earthquake, and April 7, 2011 M7.4 aftershock. Geotechnical Extreme Events Reconnaissance Report No. GEER-25. f 2011 (2011) 95pp.

[83] B. Tiwari, D. Pradel, J. Wartman, Performance of slopes and dams in The M_w 9.0 Tohoku Japan earthquake. Second International conference on Performance-based Design in Earthquake Geotechnical Engineering. Paper No. 8.06 (2012) 11pp.

[84] R. Moussa, Criteria for the choice of flood routing methods in natural channels with overbank flows. Proceedings of wetHYDRO Workshop3 (2004) 73-82.

[85] S. Grimaldi, D. Poggi, A synthetic method for assessing small dams flood wave. River Flow 2010 (2010) 631-639.

Table 1: Dimensions of the main and auxiliary embankments.

Dam dimension	Main embankment	Auxiliary embankment
Crest height (m)	18.5	15.0
Crest length (m)	133	60
Crest width (m)	6	*n.a.*
Slope gradient on the upstream side	1:2.8	*n.a.*
Slope gradient on the downstream side	1:2.5	*n.a.*

n.a. Not available
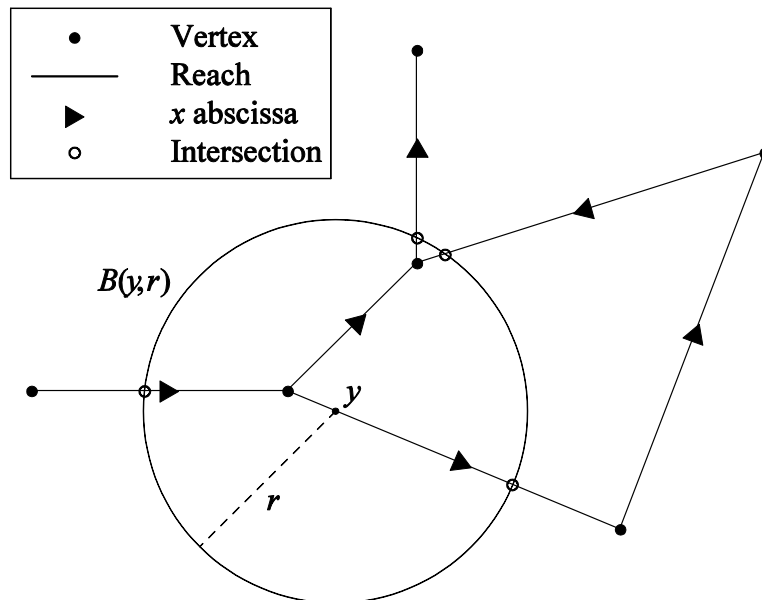
Figure 1: Schematic diagram of $B(y,r)$ for the continuity equation (4).
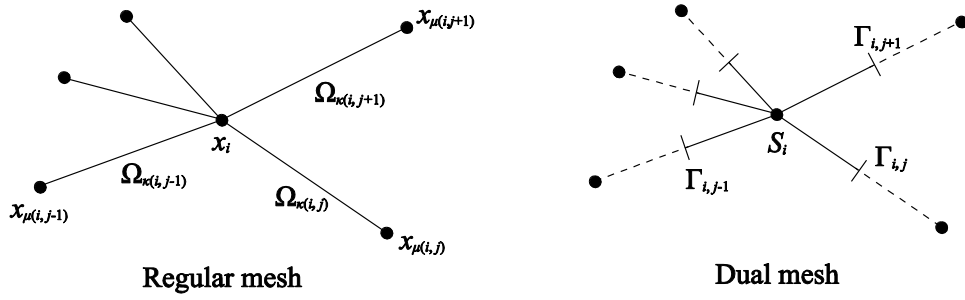
Figure 2: Schematic diagrams of a regular mesh and a dual mesh.
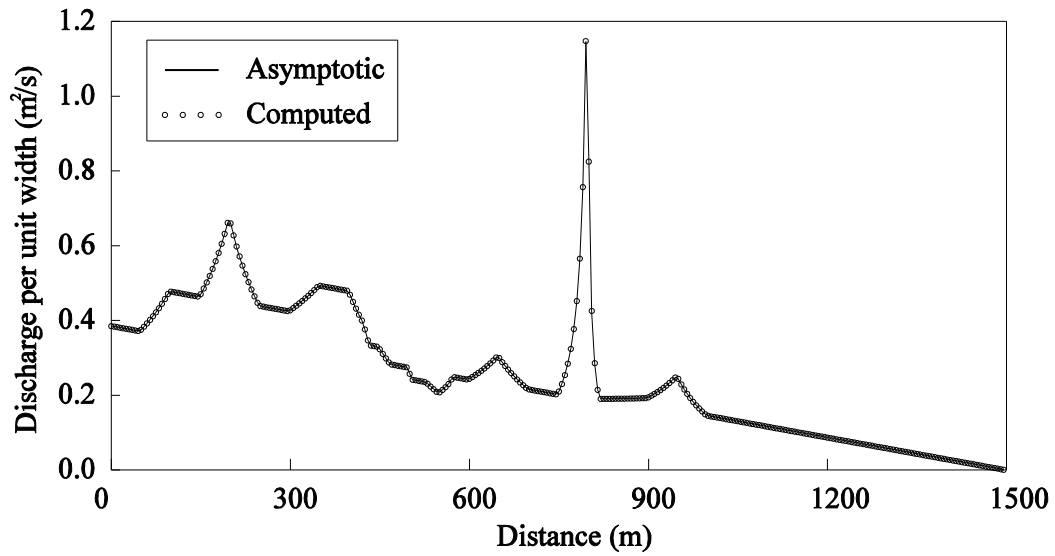
Figure 3: Comparison of the analytical and computed discharges per unit width solving the tidal wave problem solving the complex bathymetry.
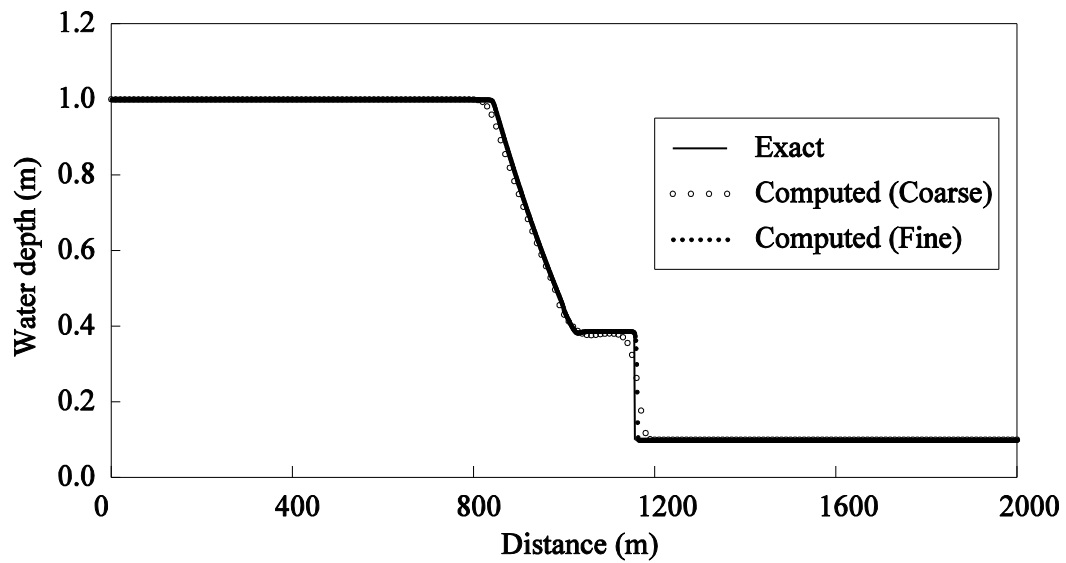
Figure 4: Comparison of the exact and computed water surface profiles of the dam break problems in a rectangular channel (Case DB-A).

30
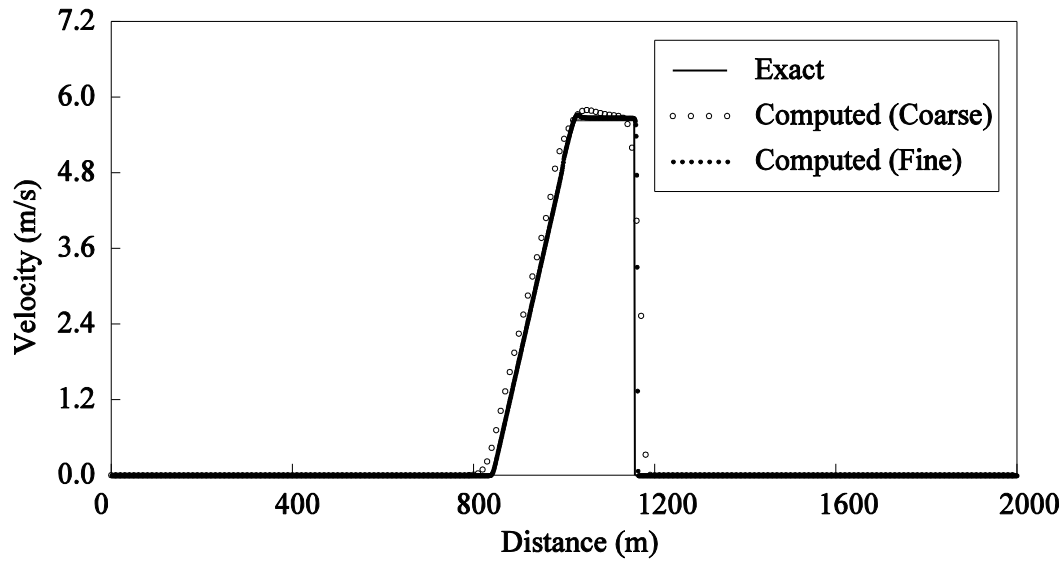
Figure 5: Comparison of the exact and computed velocity distributions of the dam break problems in a rectangular channel (Case DB-A).
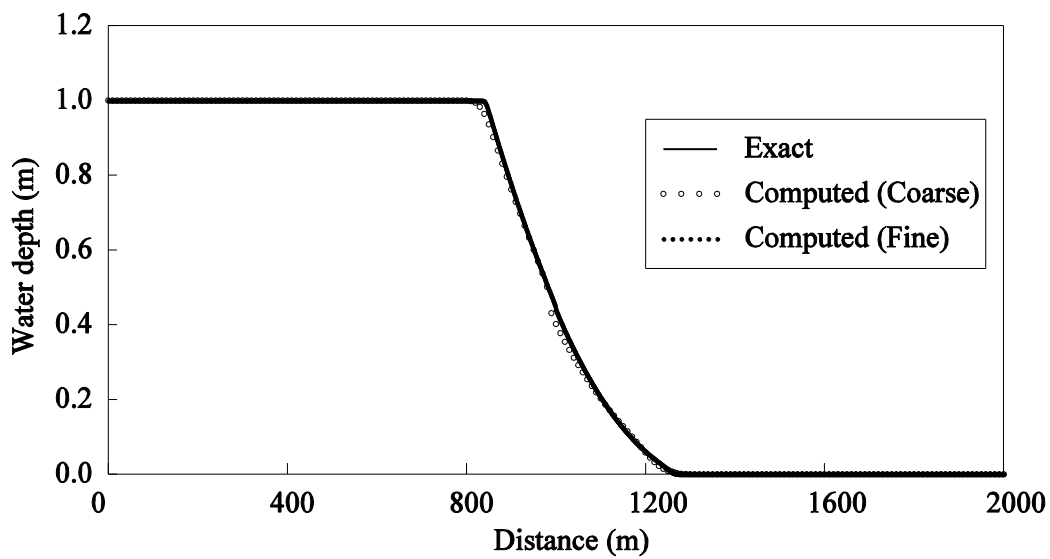
Figure 6: Comparison of the exact and computed water surface profiles of the dam break problems in a rectangular channel (Case DB-B).
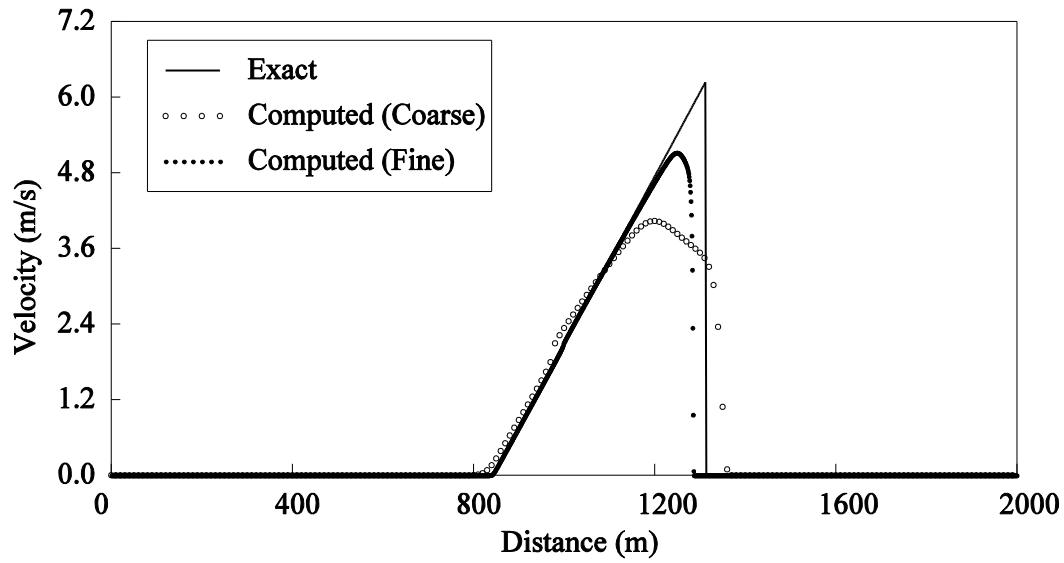
Figure 7: Comparison of the exact and computed velocity distributions of the dam break problems in a rectangular channel (Case DB-B).
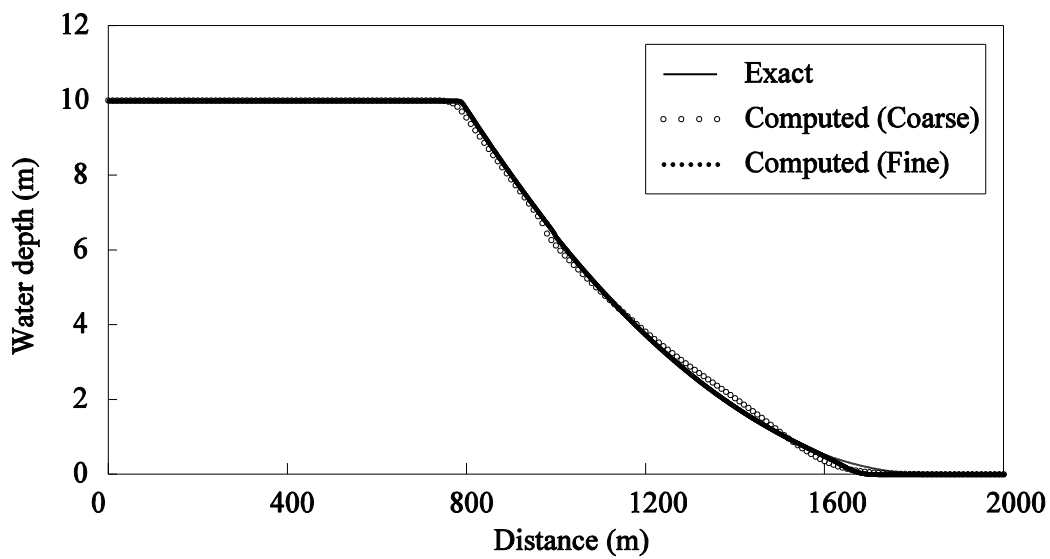
Figure 8: Comparison of the exact and computed water surface profiles of the dam break problem in a triangular channel.
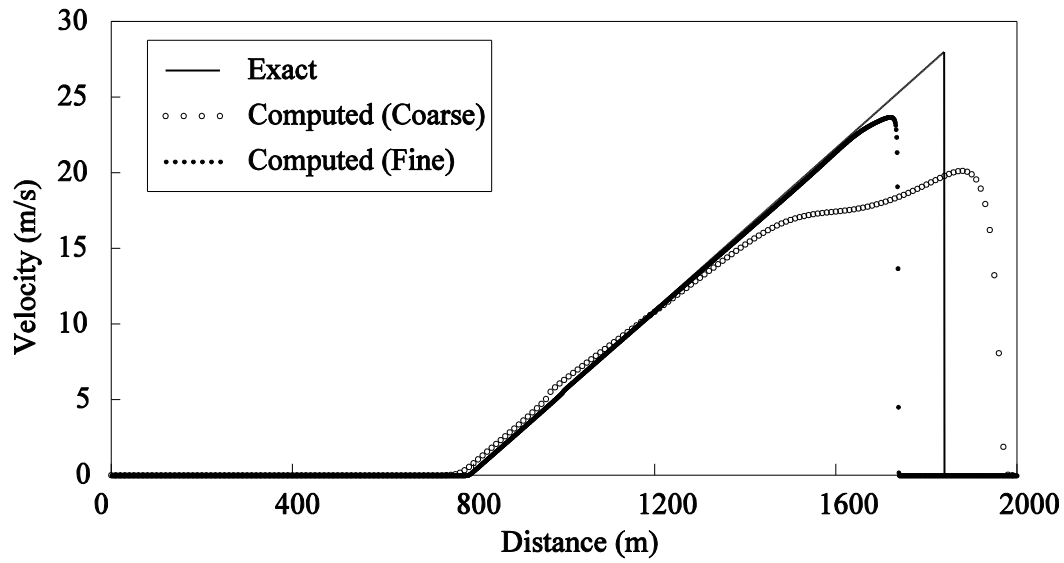
Figure 9: Comparison of the exact and computed velocity distributions of the dam break problem in a triangular channel.
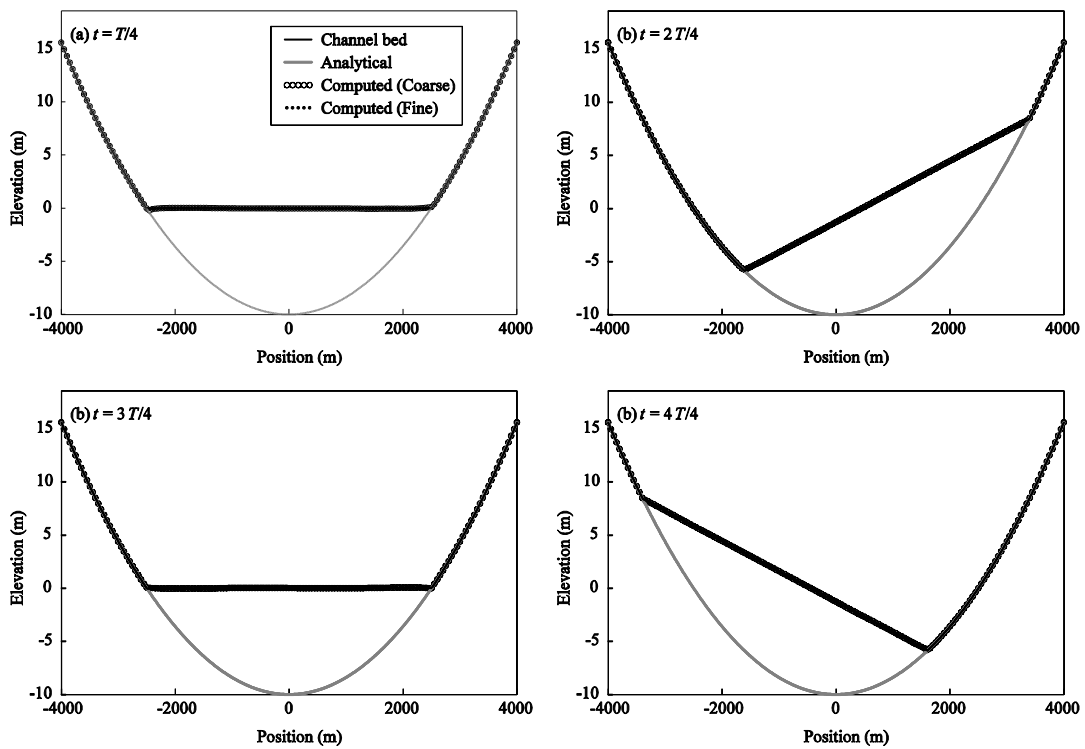
Figure 10: Comparisons of the exact and computed water surface profiles for the Thacker's test case.
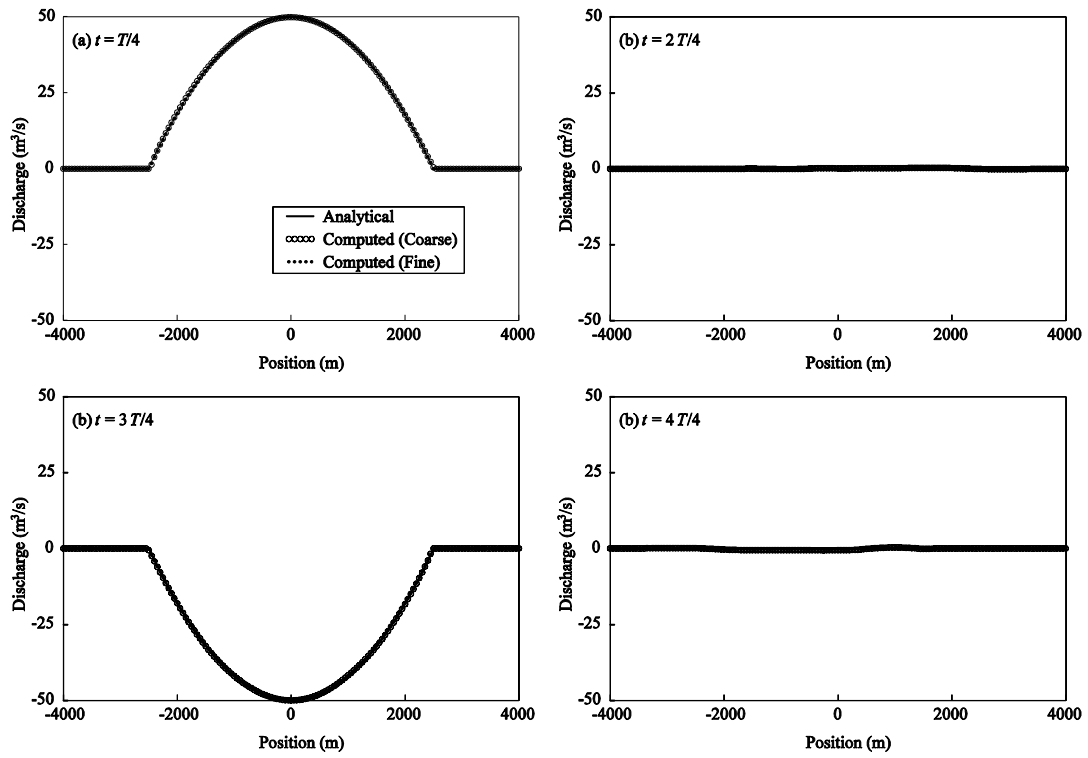
Figure 11: Comparisons of the exact and computed discharges for the Thacker's test case.
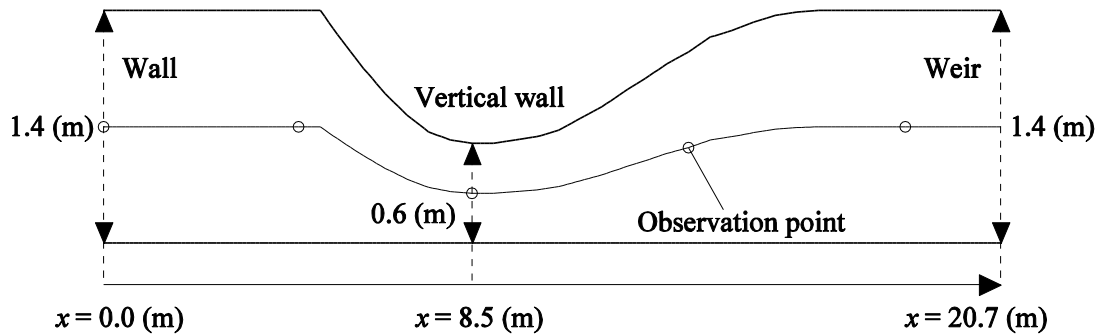
Figure 12: Schematic diagram of the dam break problem in a non-prismatic experimental channel.
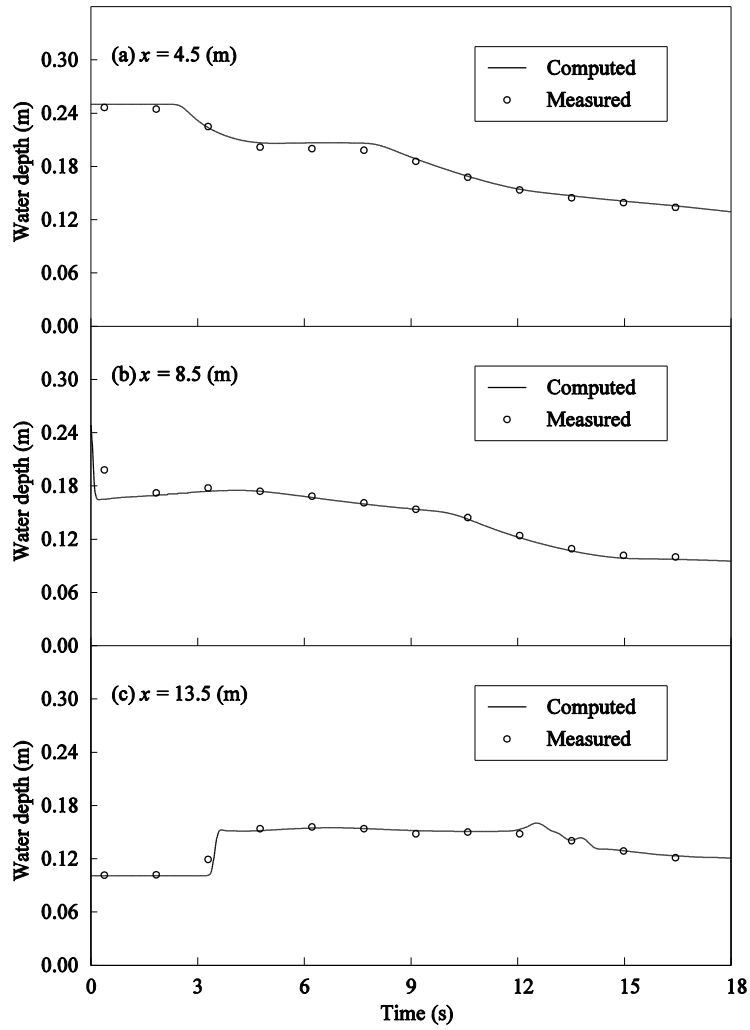
Figure 13: Comparisons of the computed and measured water depths at each observation point for the dam break problem in a non-prismatic experimental channel.
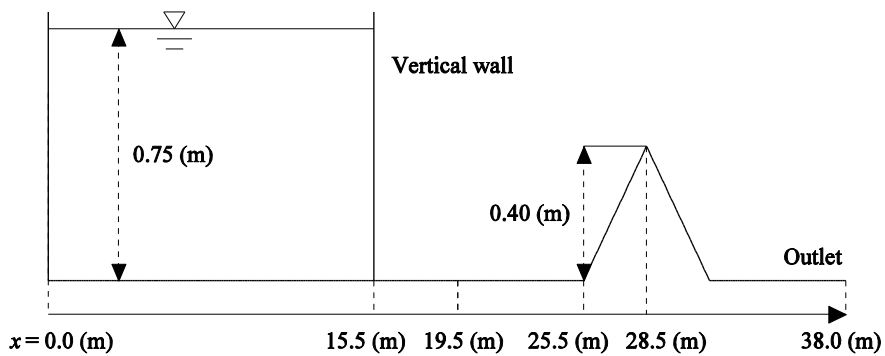
Figure 14: Schematic diagram of the dam break problem with a triangular bump.

35
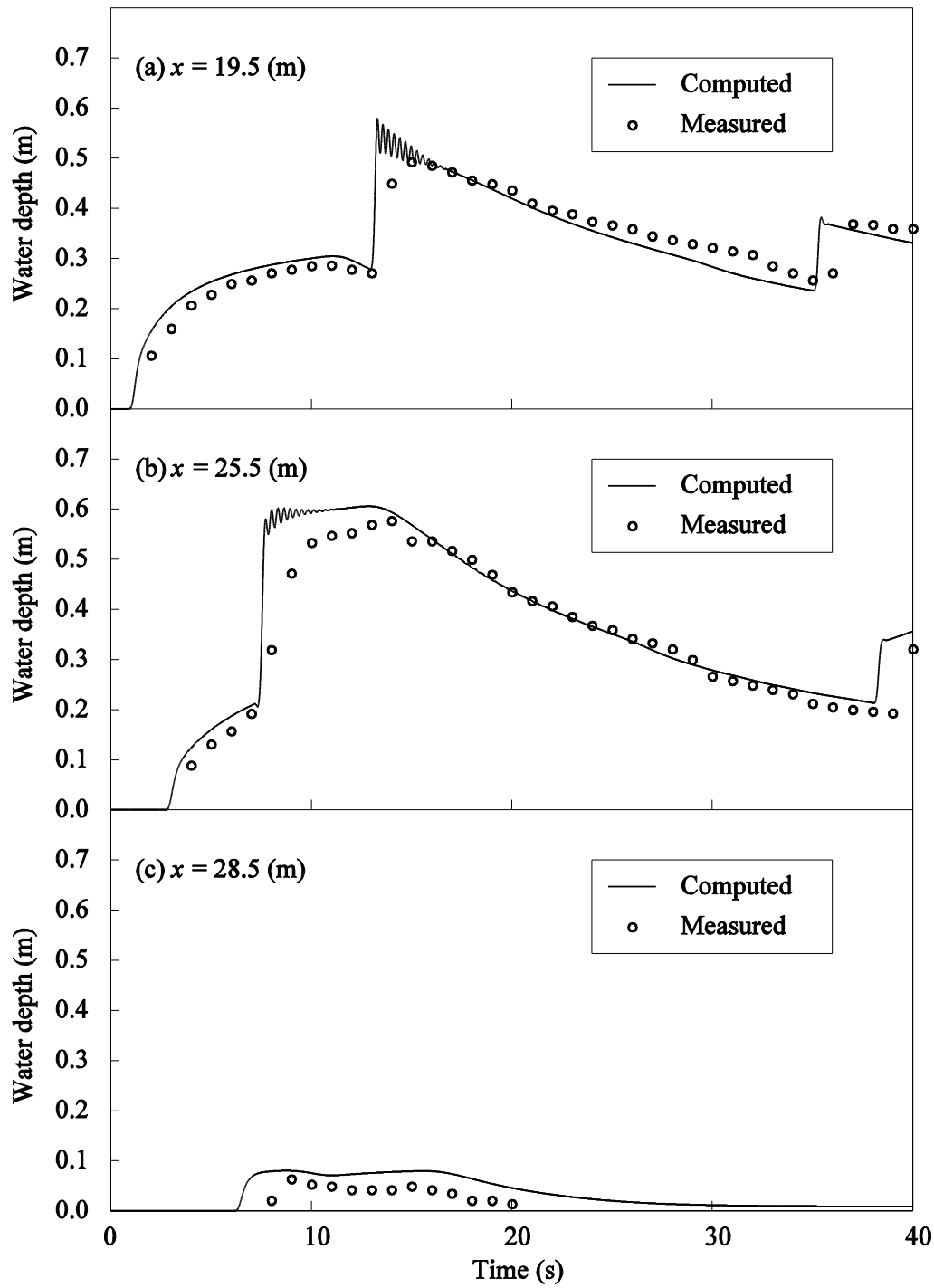
Figure 15: Comparisons of the computed and measured water depths at each observation point for the dam break problem with a triangular bump.
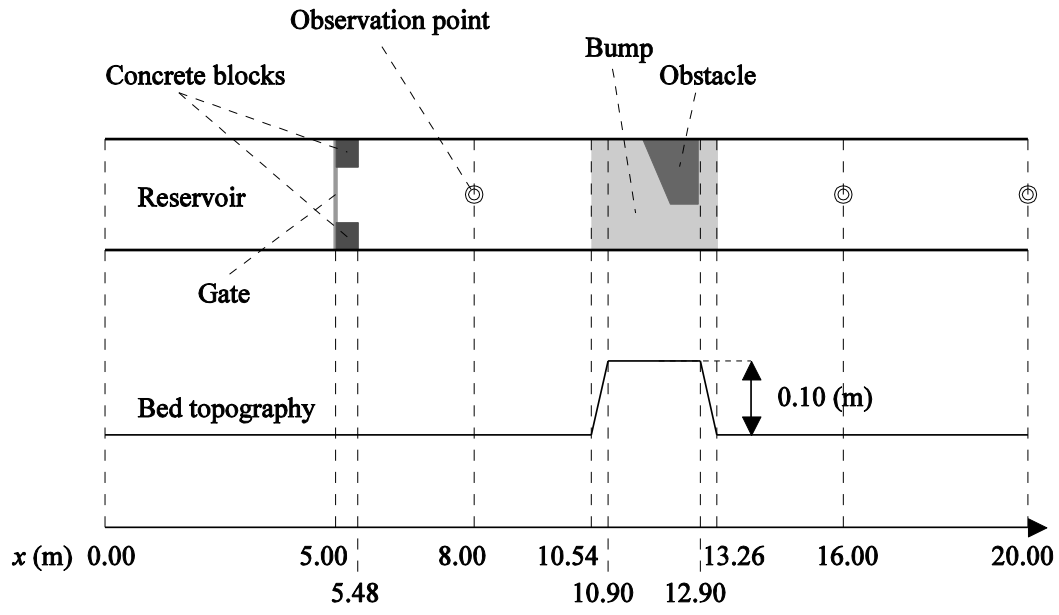
Figure 16: Schematic sketch of the experimental channel for the dam beak problems in a non-prismatic and non-flat channel.
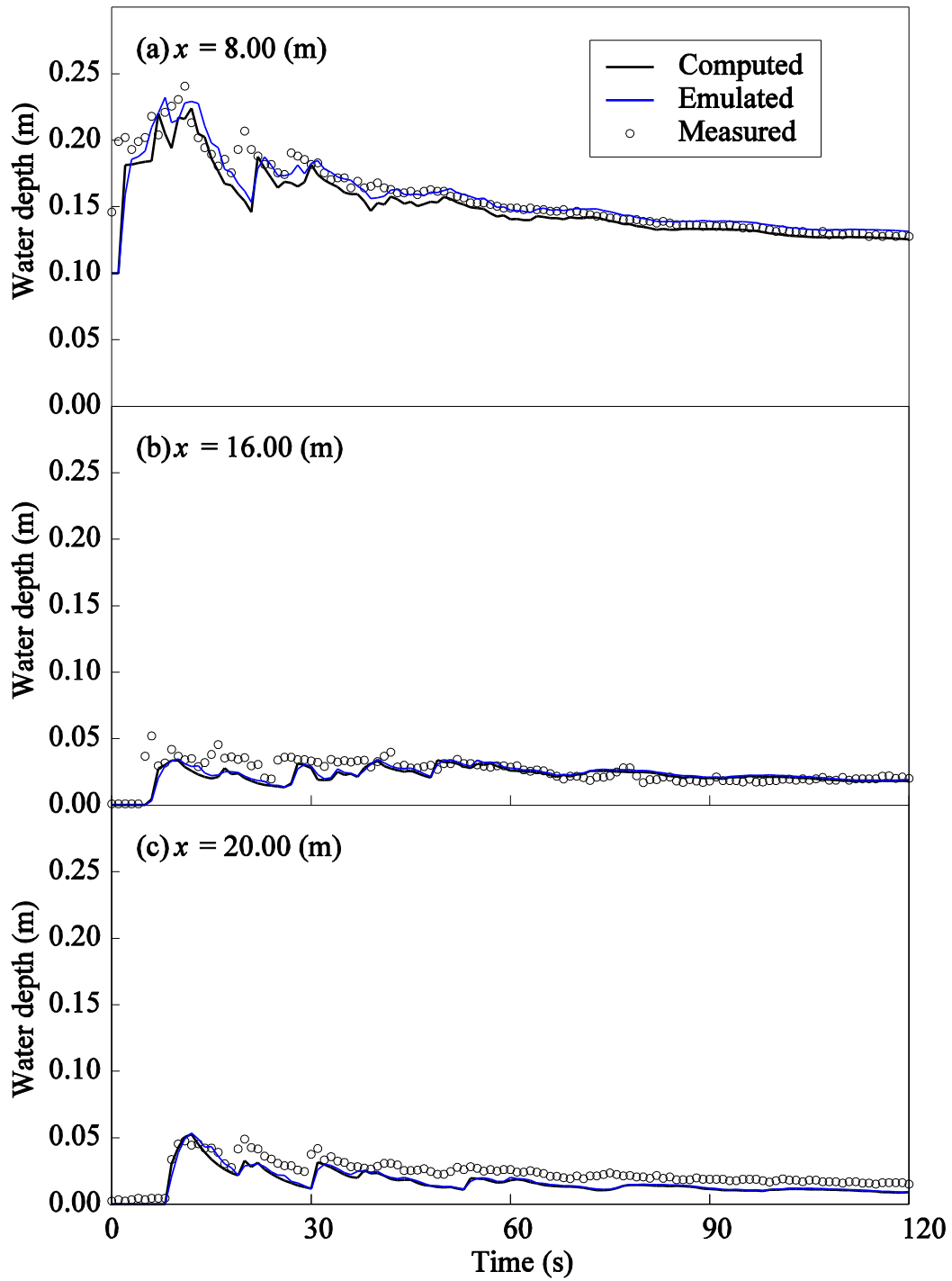
Figure 17: Comparisons of the computed, emulated, and measured water depths at each station with the slope $S = 0$.
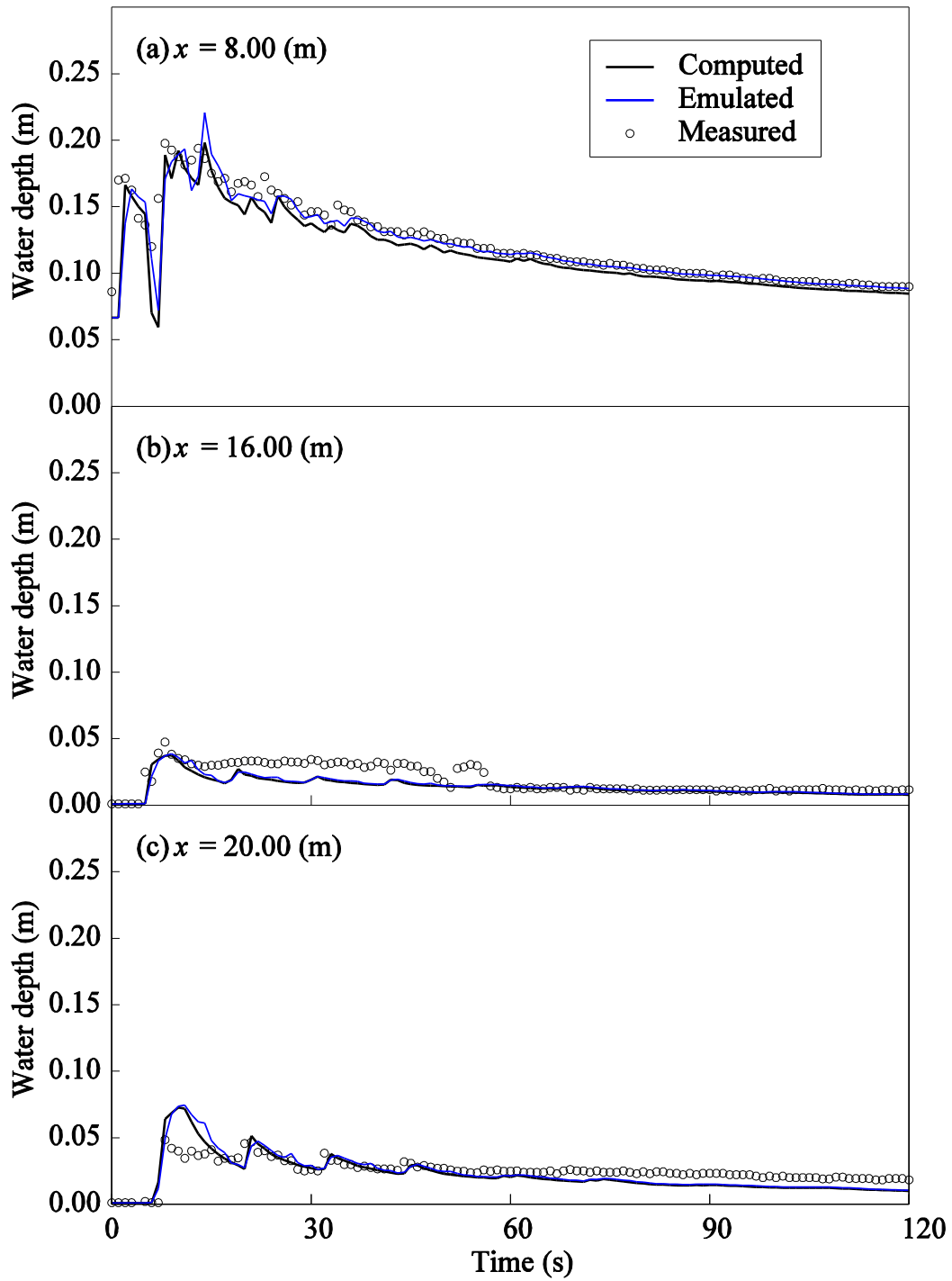
Figure 18: Comparisons of the computed, emulated, and measured water depths at each station with the slope $S = 0.01$.
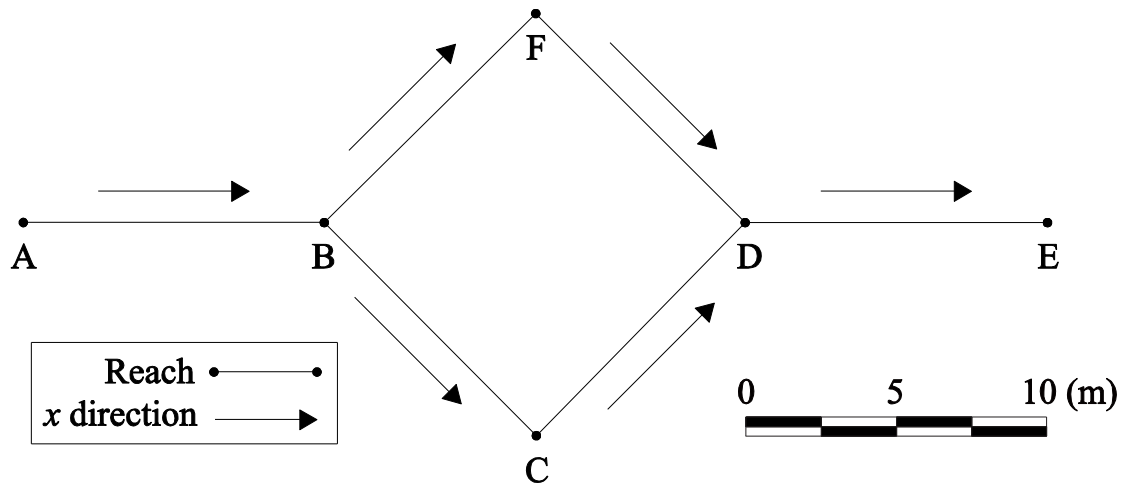
Figure 19: Schematic diagram of the hypothetical multiply connected channel network with key nodes.
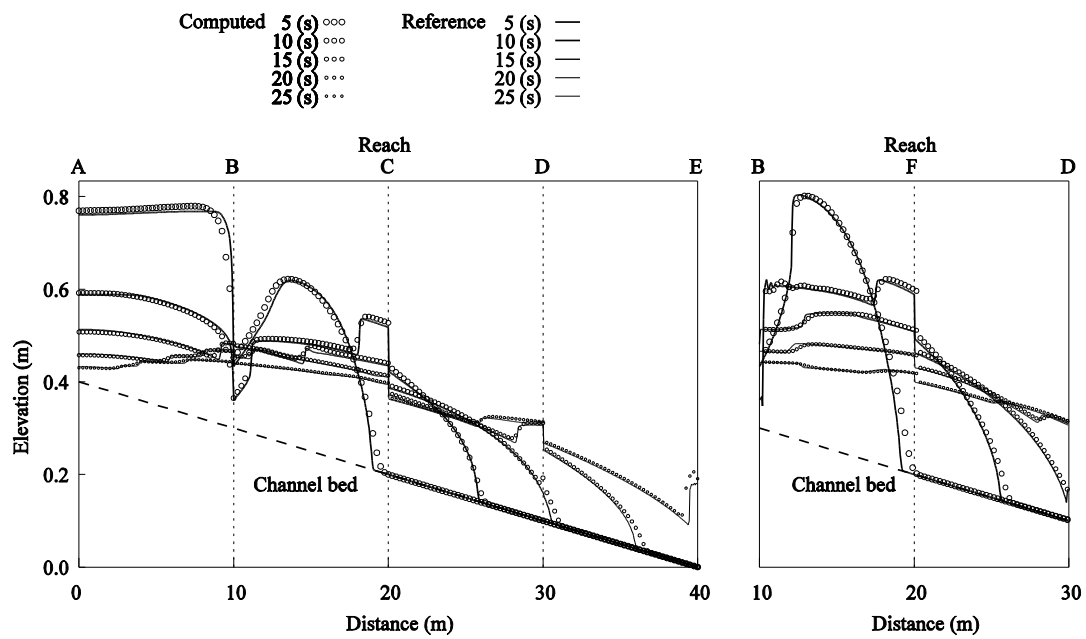
Figure 20: Comparisons of the computed and reference water surface profiles in reaches A-B-C-D-E and B-F-D at each time step for the dam break problem in a multiply connected channel network with a rectangular cross-section.
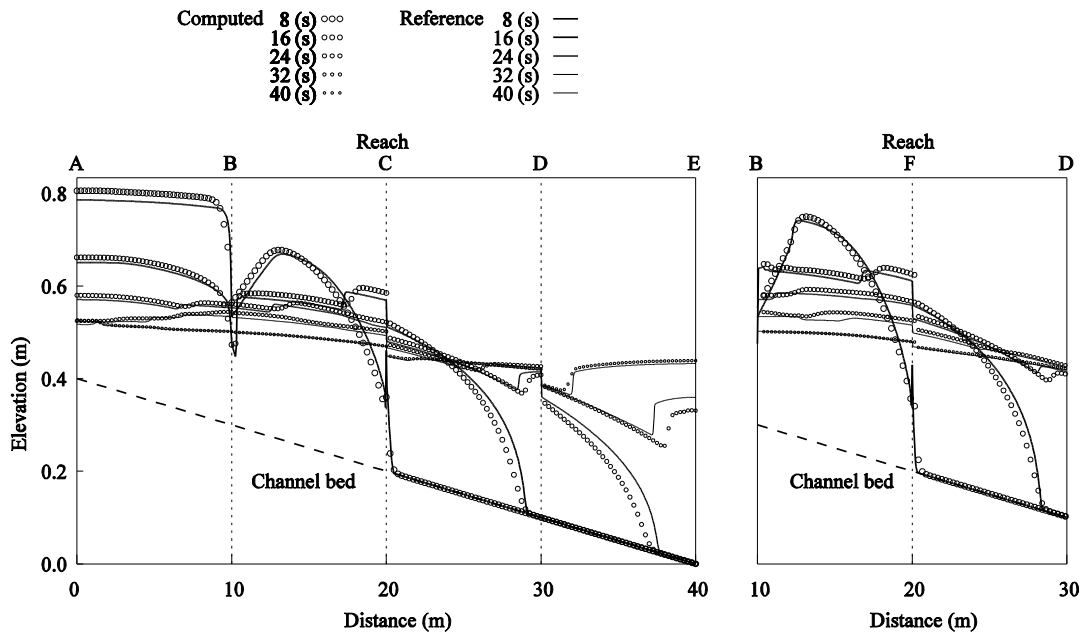
Figure 21: Comparisons of the computed and reference water surface profiles in reaches A-B-C-D-E and B-F-D at each time step for the dam break problem in a multiply connected channel network with a triangular cross-section.
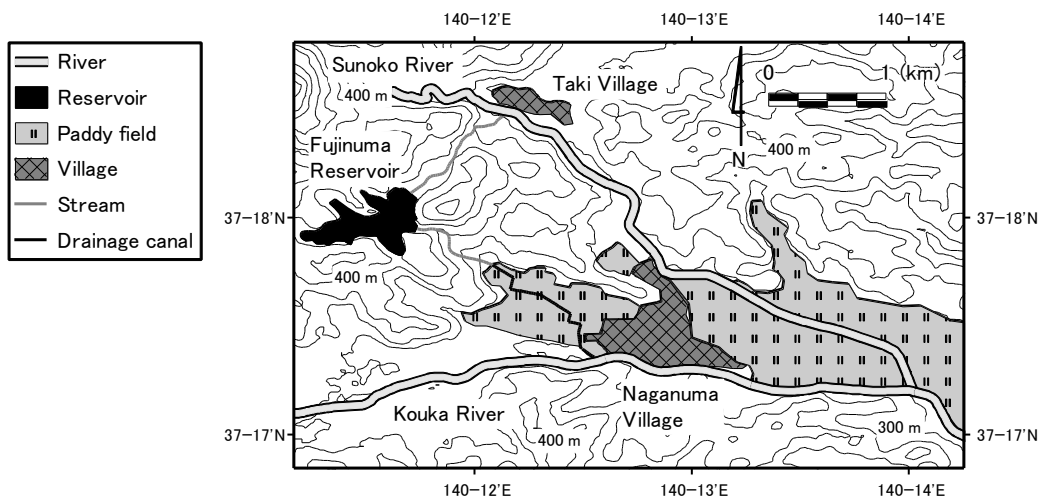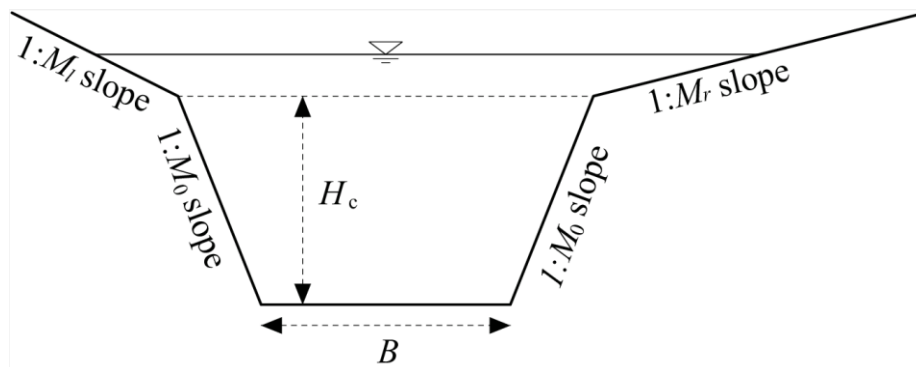

Figure 22: Map of the study area.
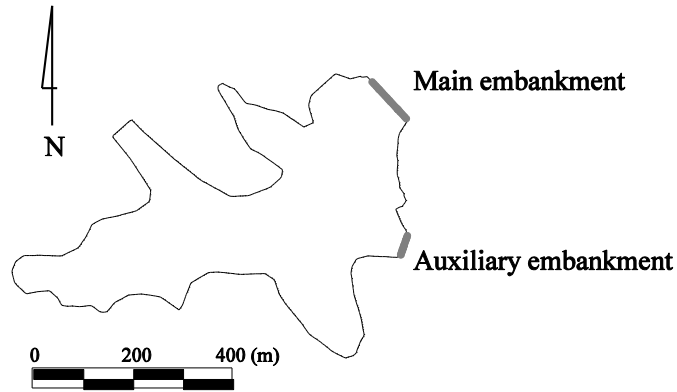
Figure 23: Sketch of Fujinuma Dam.
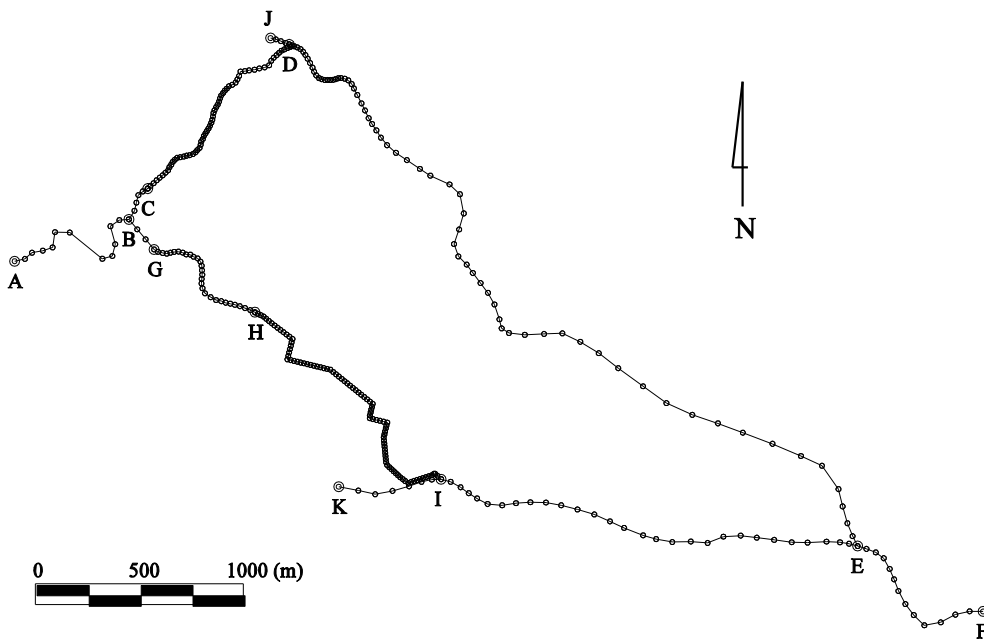
Figure 24: Schematic diagram of the computational domain with key nodes for the flood caused by the Fujinuma Dam failure.

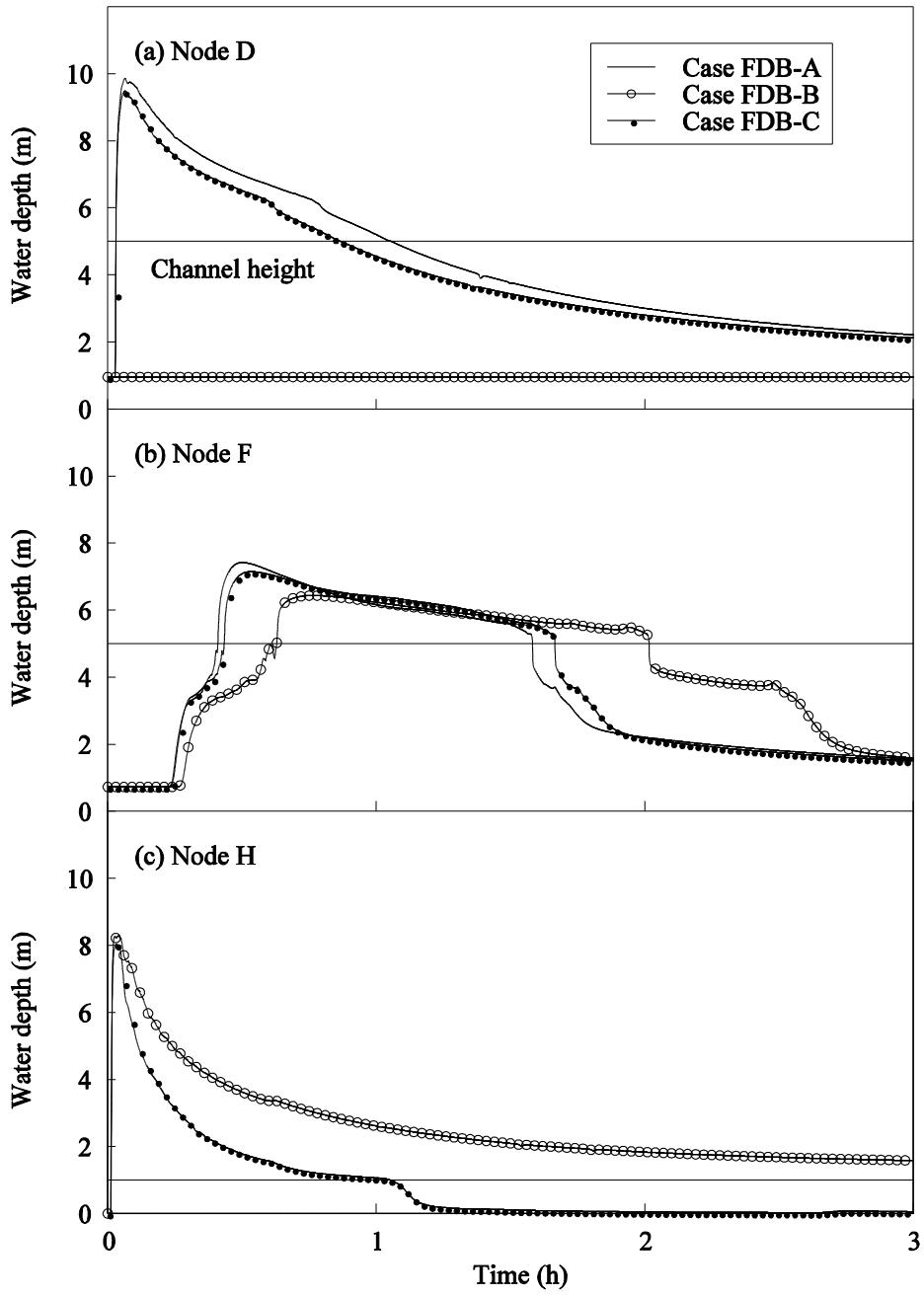**Figure 25:** Schematic diagram of each channel cross-section in the study area.

Figure 26: Hydrographs at nodes D, F, and H for each case.

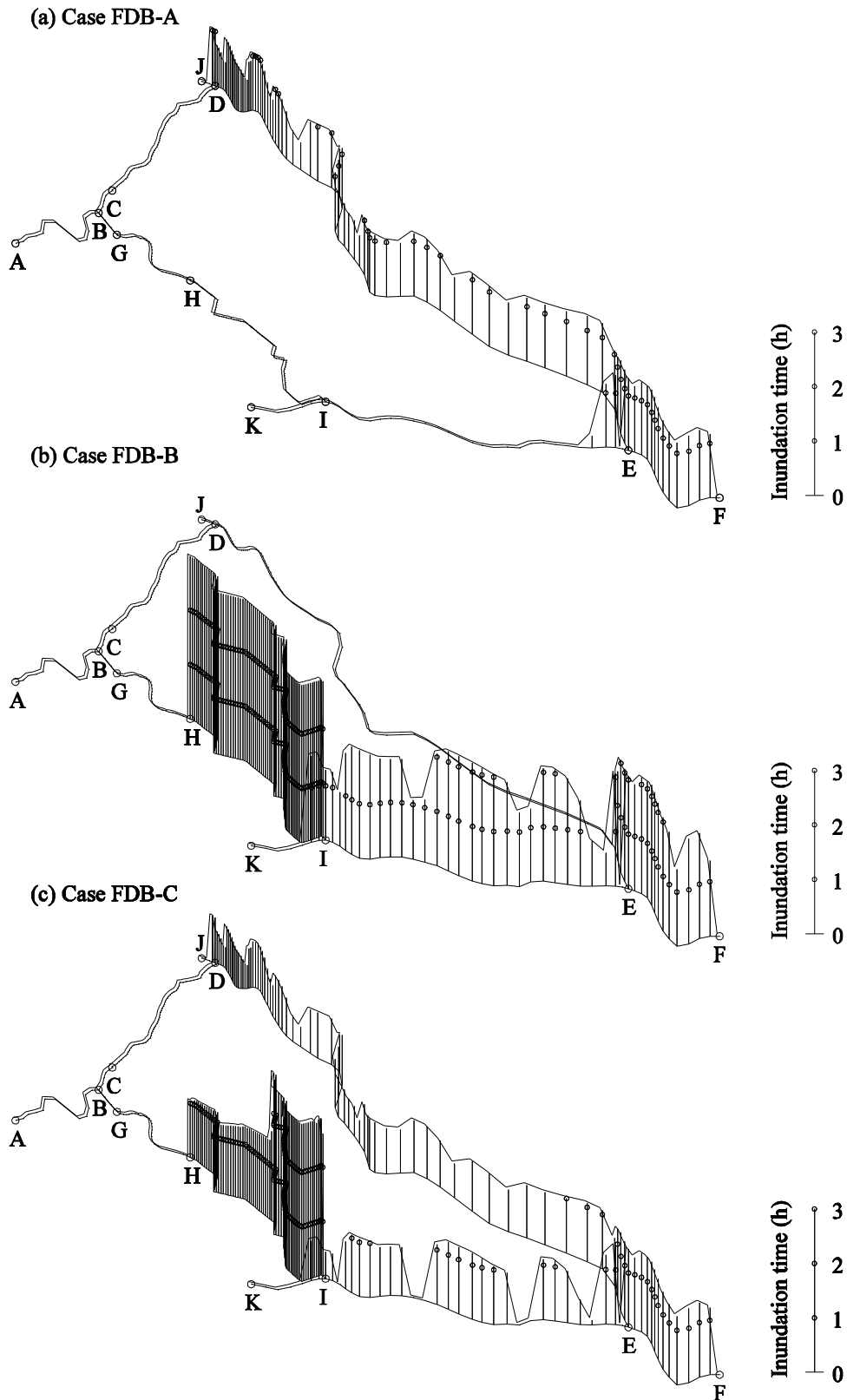**Figure 27:** Water surface profiles in the channel network at each time step for Case FDB-C.

Figure 28: Inundation time distribution in the channel network for each case.

Figure 29: Inundation map for each case.